

RESEARCH ARTICLE | NOVEMBER 19 2024

New insights into the dissolution mechanisms of iron oxides and combusted iron particles in oxalic acid

M. Lausch ; A. Zimina ; J. Bao ; R. Pashminehazar ; B. J. M. Etzold ; U. I. Kramm ;
J.-D. Grunwaldt ; J. Hussong 



J. Chem. Phys. 161, 194308 (2024)

<https://doi.org/10.1063/5.0229410>



View
Online



Export
Citation

Articles You May Be Interested In

Substrates of anodic Alumina as the basis of detectors

AIP Conference Proceedings (November 2021)

Recycle of scrap plutonium-238 oxide fuel to support future radioisotope applications

AIP Conference Proceedings (January 1998)

Study of the synthesis NMC-622 cathode active material with oxalate coprecipitation method at different reaction time

AIP Conf. Proc. (May 2023)



The Journal of Chemical Physics

Special Topics Open for Submissions

[Learn More](#)

New insights into the dissolution mechanisms of iron oxides and combusted iron particles in oxalic acid

Cite as: J. Chem. Phys. 161, 194308 (2024); doi: 10.1063/5.0229410

Submitted: 18 July 2024 • Accepted: 22 October 2024 •

Published Online: 19 November 2024



View Online



Export Citation



CrossMark

M. Lausch,^{1,a)} A. Zimina,^{2,3} J. Bao,⁴ R. Pashminehazar,^{2,3} B. J. M. Etzold,^{5,6} U. I. Kramm,⁴ J.-D. Grunwaldt,^{2,3} and J. Hussong¹

AFFILIATIONS

¹Technische Universität Darmstadt, Institute for Fluid Mechanics and Aerodynamics, 64347 Griesheim, Germany

²Karlsruhe Institute of Technology, Institute of Catalysis Research and Technology, 76344 Eggenstein-Leopoldshafen, Germany

³Karlsruhe Institute of Technology, Institute for Chemical Technology and Polymer Chemistry, 76131 Karlsruhe, Germany

⁴Technische Universität Darmstadt, Institute for Catalysts and Electrocatalysts, 64287 Darmstadt, Germany

⁵Technische Universität Darmstadt, Ernst-Berl-Institute for Technical Chemistry and Macromolecular Science, 64287 Darmstadt, Germany

⁶Friedrich-Alexander-Universität Erlangen-Nürnberg, Power-To-X Technologies, 90762 Fürth, Germany

^{a)} Author to whom correspondence should be addressed: lausch@sla.tu-darmstadt.de

ABSTRACT

The influence of oxidation state and crystalline structure on the dissolution mechanisms of both pure iron oxides and combusted iron particles in aqueous oxalic acid (0.5 mol/l) at 60 °C was systematically investigated. Dissolution experiments were carried out in a temperature-controlled, continuous-flow capillary reactor, allowing for the removal of reaction products and thereby suppressing the autocatalytic reaction mechanism. The non-reductive dissolution of α -Fe₂O₃ was observed through *in situ* x-ray absorption measurements. In contrast, the dissolution of spinel-type oxides such as γ -Fe₂O₃ and Fe₃O₄ proceeded reductively, indicated by gradual changes in characteristic spectral features. Given that γ -Fe₂O₃ and Fe₃O₄ share a similar crystal structure but differ in the nominal oxidation state, this implies that the phase composition is decisive for the reductive dissolution. For mixed-phase particles consisting of spinel and rhombohedral phases (maghemite and hematite), the preferential dissolution of the spinel phase was observed. Despite the similar bulk composition of spinel and rhombohedral phases in the combusted iron particles (as confirmed by Mössbauer spectroscopy and x-ray diffraction analysis), dissolution predominantly follows a non-reductive pathway, with no preferential dissolution of the γ -phase. This unique dissolution behavior of combusted iron particles arises from their layered microstructure.

© 2024 Author(s). All article content, except where otherwise noted, is licensed under a Creative Commons Attribution-NonCommercial-NoDerivs 4.0 International (CC BY-NC-ND) license (<https://creativecommons.org/licenses/by-nc-nd/4.0/>). <https://doi.org/10.1063/5.0229410>

I. INTRODUCTION

Understanding the microscopic phenomena during iron oxide dissolution is crucial for optimizing industrial processes such as corrosion product removal^{1–3} and iron ore leaching.^{4–6} These insights are vital for developing sustainable electrochemical reduction methods in steelmaking, a significant contributor to global energy use and CO₂ emissions.^{7,8} This process includes leaching, using the liquid product as an electrolyte in electrolysis, and recovering metal from the cathode. Iron reduction by this

method could also support a green metal fuel economy, where metals such as iron, favored for its abundance and stability, act as energy carriers.^{7,9–13} The energy is released by combusting iron particles, followed by the reduction of the resulting oxides using renewable energy.^{7,10} Oxalic acid (OxA) is highly efficient for iron oxide dissolution^{14–16} and is also used in deep eutectic solvents,¹⁷ potentially allowing insights from aqueous dissolution to apply to non-aqueous systems. Non-aqueous solvents, lacking hydrogen evolution reaction, could enhance the efficiency of electrochemical reduction.

The dissolution of iron oxides in OxA involves multiple mechanisms, summarized extensively in the literature.^{18–22} After protonation and the formation of an iron-oxalate complex on the particle surface,^{21,23} two pathways occur. The first, non-reducing, involves iron detachment due to Fe–O bond weakening during protonation or surface complex reaction with a proton, leading to desorption.^{21,23,24} The second is the reduction of Fe^{III} to Fe^{II} by electron transfer from an oxalate ion, weakening the iron–oxygen bond and facilitating detachment.^{23,25,26} This contribution of the reductive pathway increases in general with lower temperatures, lower OxA concentrations, higher pH, and higher Fe²⁺ ion concentrations.^{21,23} The ferrous ions, either from reductive dissolution or external addition, can drive an autocatalytic reaction, where Fe²⁺ oxalate complexes in solution transfer electrons to Fe^{III} ions on the surface.^{21,23} Short-wavelength light can also reduce aqueous Fe³⁺ complexes via photolysis or, due to the semiconductor properties of iron oxides, reduce lattice iron directly or ligand-promoted.^{20,27–30} These semiconductors combined with magnetic properties are particularly advantageous for ferrites, making them effective as recoverable photocatalysts.^{31–33} The pH, ionic strength, and OxA concentration influence oxalate ion species distribution,^{34,35} governing the species participating in the reaction. If ferrous iron and doubly deprotonated oxalate ions are present, iron(II) oxalate dihydrate (humboldtine) precipitate can form.³⁶ Iron(II) oxalate is stable between pH 1.6 and 3.2 according to Lee *et al.*¹⁵ but has been observed at lower pH values.^{36,37} In fact, without active pH control, its formation remains stable regardless of OxA concentration.^{19,21,38} However, despite its importance for leaching applications, its nucleation site is still unclear, with some evidence pointing to formation at the particle surface as an inherent dissolution mechanism³⁹ and other research suggesting the homogeneous phase.^{40,41}

The crystal structure defines the semiconductor properties of iron oxides, as the distribution of the electronic states in valence and conduction bands is ruled by the interaction of the anions and cations in the solid.^{20,28} Since the bonding depends on local coordination, dissolution is not uniform across crystal sites, as noted by Lasaga and Lüttge⁴² and Valverde and Wagner.⁴³ Lasaga and Lüttge⁴² suggested a heterogeneous dissolution process where surface defects initiate dissolution waves. Preferred dissolution directions have also been observed on iron oxide surfaces.^{44,45} Moreover, the semiconductivity of iron oxides also enables electron transfer through the crystal, potentially leading to varied reaction mechanisms and site-dependent reactivity across the particle surface. For instance, Yanina and Rosso⁴⁶ used OxA on hematite (α -Fe₂O₃) crystals to create a surface potential gradient, promoting growth through the adsorption of Fe²⁺_(aq) on the (001) face while dissolving single and triple coordinated Fe^{III} on the (hk0) face. They also observed that decreasing pH increased the site-dependent open-circuit potential, attributed to the asymmetry of the (001) face compared to other faces.⁴⁷ Simultaneous growth and dissolution of different crystal faces were also demonstrated for goethite (α -FeOOH).⁴⁸ Variations in the crystal structure also affect the reaction rates, which is linked to the contribution of different reaction mechanisms. Stumm *et al.*,⁴⁹ p. 60, showed that reaction rates increase from goethite to hematite to ferrihydrite, while Litter *et al.*⁵⁰ demonstrated a faster dissolution for spinel-type maghemite (γ -Fe₂O₃) compared to rhombohedral hematite, attributing these differences to photoreactivity and conductivity changes in the

crystal. This conclusion was supported by studies on dissolution rates in thioglycolic acid with varying Co substitutions in magnetite (Fe₃O₄).^{51,52} Even without chelating ligands, reductive dissolution has been observed for spinel oxides using sulfuric acid⁵³ or tris(picolinato)vanadium(II).⁵⁴ However, reduction is not limited to spinel structures; Santawaja *et al.*⁴⁰ and Taxiarchou *et al.*²² observed Fe²⁺ formation during hematite dissolution in the dark, indicating active reductive pathways. Similarly, Vehmaanperä *et al.*³⁶ and Vehmaanperä, Salmimies, and Häkkinen⁵⁵ suggested a reductive contribution for the dissolution of hematite, although light exposure may have influenced these results. Crucially, studies on reductive dissolution are difficult to compare due to variations in OxA concentrations—from millimolar^{50,56} to 1 mol/l⁴⁰—and differing pH adjustments, of which both significantly affect solution complexes.^{19,35} Despite evidence highlighting the role of crystal structure in electron transfer, the specific impact on the equilibrium between reaction mechanisms thus remains unclear, particularly for higher acid concentrations and temperatures relevant for industrial processes. This uncertainty is exacerbated by the use of batch experiments in the existing studies, which allow for autocatalytic reaction that further contributes to oxide reduction.

A change in the nominal oxidation state of iron oxide is often accompanied by a change in the crystal structure. However, even when crystal structures are similar, as in magnetite and maghemite, significant differences in dissolution mechanisms can arise. In maghemite, the vacant octahedral Fe²⁺ sites of magnetite result in variations in lattice energy⁵⁷ and conductivity, with magnetite being a conductor and maghemite being an insulator at room temperature.⁵⁸ The release of Fe²⁺ into solution is generally more energetically favorable than that of Fe³⁺.⁵⁹ However, reduced Fe²⁺ behaves distinctly compared to the original Fe²⁺ within the crystal. If Fe²⁺ is reduced on the surface via electron transfer, it becomes more reactive than Fe²⁺ of the original crystal.²⁶ Once an electron transfer occurs, the crystal lattice around the reduced iron destabilizes due to the loss of charge and the increased size of the reduced iron¹⁸ (p. 306).^{21,59} The increased lability of the O–Fe²⁺ bond facilitates its detachment from the crystal, leading to a faster solubilization of ferrous iron²¹ and subsequently accelerating the autocatalytic mechanism. It has been shown that electron transfer is the rate-determining step in the reductive dissolution mechanism of magnetite,⁵⁶ not the detachment of Fe²⁺ as suggested by Cornell and Schwertmann.¹⁸ Depending on the electronic structure, ferrous ions that activate the autocatalytic reaction cycle can originate from the crystal itself, as in magnetite or wüstite (FeO), or stem from the reduction of surface Fe^{III}, as in hematite or maghemite. Particularly for magnetite, faster dissolution has been observed,^{36,37} which is still faster than that of maghemite.²³ Thus, the oxidation state influences reaction mechanisms both directly, through changes in dissolution-governing particle properties, and indirectly, by activating autocatalysis depending on the initial Fe²⁺ fraction in the crystal.

The influence of mixed phases on dissolution is less explored compared to pure iron oxides, so far mostly in the context of purification of clay materials such as kaolin.^{6,60–62} The dissolution of iron rust (consisting of hematite and iron hydroxides) in OxA has been observed to occur more rapidly than with pure hematite. This increased dissolution rate was attributed to the absence of a passivating ferrous oxalate layer that was speculated to form on hematite

particles.¹⁵ The literature describes the addition of Fe^{2+} either in salt form^{6,60} or through magnetite⁶¹ as a method to initiate the autocatalytic reaction mechanism. While the resulting dissolution then involves mixed phases in the reaction vessel, a detailed understanding of the mechanisms within a single mixed-phase particle remains lacking. However, given the described influence of crystal structure and oxidation state on semiconducting properties and reaction mechanisms, a mixed phase could significantly impact the dissolution behavior. For example, Nakanishi *et al.*⁶³ demonstrated enhanced photocatalytic activity upon introducing a γ -phase into a hematite crystal, which is typically in the α -phase.

In conclusion, while a substantial body of literature addresses iron oxide dissolution mechanisms, significant gaps remain in our understanding of the factors that govern their equilibrium. Most studies have primarily explored the effects of light on the reduction of iron oxides due to their semiconducting properties, rather than on the particular effect and interaction between particle characteristics, such as crystal structure or nominal oxidation state, on the occurring dissolution mechanisms. Although the reductive pathway for spinel-type oxides has been documented, disentangling individual influences proves challenging due to the complex interplay of the outlined reaction mechanisms. In addition, variations in the crystal structure often coincide with changes in the nominal oxidation state, which can also affect the equilibrium (e.g., hematite vs magnetite). Moreover, existing studies typically involve batch experiments, leading to self-interaction with reaction products and vessel size-dependent concentration effects. Research on mixed-phase iron oxide dissolution is particularly scarce; however, understanding its influence on dissolution mechanisms is crucial for potential electrochemical reduction applications in the context of recyclable metal fuels.

To close these gaps, the objective of this study is to systematically investigate the influence of crystal structure and oxidation state on the equilibrium between reductive and non-reductive reaction mechanisms. Besides pure iron oxides, this includes mixed-phase iron oxides such as combusted iron particles (CIPs) in the context of recyclable metal fuels, with their phase composition and oxidation state varying depending on combustion boundary conditions.^{64–66} To overcome the limitations of previous studies, a continuous-flow setup was utilized, allowing the removal of reaction products and eliminating autocatalytic effects. Advanced *in situ* x-ray absorption spectroscopy (XAS) was applied in combination with *ex situ* x-ray diffraction (XRD), Mössbauer spectroscopy, scanning electron microscopy (SEM), and x-ray tomography.

II. MATERIALS AND METHODS

A. Chemicals

The OxA concentration is constant for all experiments at 0.5 mol/l (obtained from Chem-Lab, Belgium), selected so that the molar ratio is well above the minimum required for complete dissolution ($c_{\text{H}_2\text{C}_2\text{O}_4}/c_{\text{Fe}} \approx 1.82$ according to Santawaja *et al.*³⁷). In addition, it yields reasonable dissolution times at elevated temperatures, as established through preliminary tests. For dissolution, five different commercial reference iron oxide particles were obtained: hematite, $\alpha\text{-Fe}_2\text{O}_3$ [Alfa Aesar, iron(III) oxide, 99.9% (metal basis)]; maghemite, $\gamma\text{-Fe}_2\text{O}_3$ [Alfa Aesar, iron(III) oxide, magnetic]; Fe_2O_3 (Nanografi, 325 mesh maghemite, purity 99.9+%),

which was determined as a mixture of $\alpha\text{-Fe}_2\text{O}_3$ and $\gamma\text{-Fe}_2\text{O}_3$ (see Sec. III A) denoted as $\alpha/\gamma\text{-Fe}_2\text{O}_3$; and magnetite, Fe_3O_4 (Nanografi, 325 mesh magnetite, purity 99.9+%). In addition, combusted iron particles (CIPs) from iron powder–air flames in a tube burner at a constant mean outlet velocity of 35 cm/s⁶⁷ were obtained at the first separation stage with five different fuel-to-air equivalence ratios Φ of 0.67, 0.8, 1.0, 1.25, and 1.5. For the calculation of Φ , the total conversion of iron to Fe_2O_3 is assumed. As shown in Sec. III A, however, the conversion rate, i.e., the degree of oxidation and, therefore, the phase composition of the particles, is a function of Φ .⁶⁴ For the XAS measurements, the powders were diluted with fine fused silica particles (1:20 ratio, grain size below 10 μm), grained, and sieved to the 100–200 μm fraction to minimize the self-absorption effects and to ensure the sufficient feed flow through the powder.

Additional reference samples were obtained of wüstite, FeO [Thermo Scientific Chemicals, iron(II) oxide, 99.5%]; cementite, Fe_3C (prepared according to Ref. 68 termed Fe/Aerosil-975C-CH4); and humboldtine, $(\text{Fe}^{\text{II}}\text{C}_2\text{O}_4 \cdot 2\text{H}_2\text{O})$ [Thermo Scientific Chemicals, iron(II) oxalate dihydrate, 99%], diluted with cellulose and pressed into pellets. These samples were not used for dissolution experiments.

B. Experimental setup and procedure

The chemical state of Fe in different oxides and combusted particles was monitored during their dissolution in a continuous flow of OxA through a capillary microreactor (schematic view is shown in Fig. 1) by recording the x-ray absorption near-edge structure (XANES) spectra in transmission and fluorescence modes at the CAT-ACT beamline⁶⁹ at the KIT Light Source (Karlsruhe, Germany).⁷⁰ For measurements performed in transmission mode, the incoming monochromatic intensity was measured using the first ionization chamber (IC), I_0 (6 in Fig. 1). To calculate the absorption coefficient according to the Lambert–Beer law, the intensity at I_1 (11) was used after the x-ray beam with a spot size of $\sim 2 \times 1 \text{ mm}^2$ passed the sample placed between the first and second ICs. A Fe foil (12) between the second and third ICs (13) allowed the simultaneous measurement of the iron spectrum and the subsequent calibration by setting the first inflection point of the first derivative to the tabulated value of the Fe K-edge at 7112 eV. The Fe K absorption edge is defined as the sharp rise in absorption once the x-ray energy reaches the binding energy of the 1s core electrons.⁷¹ During the *ex situ* measurement, the double-crystal Si (111) monochromator was operated in step scanning mode with data point acquisition in 0.3 eV increments in the range of ± 30 eV at the Fe K-edge and monotonically increasing increments of 1–4.7 eV from 30 eV up to at least 1000 eV above the Fe K-edge. These scanning parameters were chosen to capture the spectral features while minimizing measurement time and are referred to as Long-Scans (LS). The scans were performed for the reference pellets of the oxides described in Sec. II A and prior to the dissolution experiments for the prepared, dry particles in the capillary (4). Since the combusted iron particles can exceed 20 μm in diameter, absorption of some of the oxides in the capillary was expected and causes significant self-absorption distortions in the transmission XANES data. For such cases, an energy-dispersive one-element solid-state Si detector (5) was used to simultaneously measure the spectra in fluorescence mode.

Top view

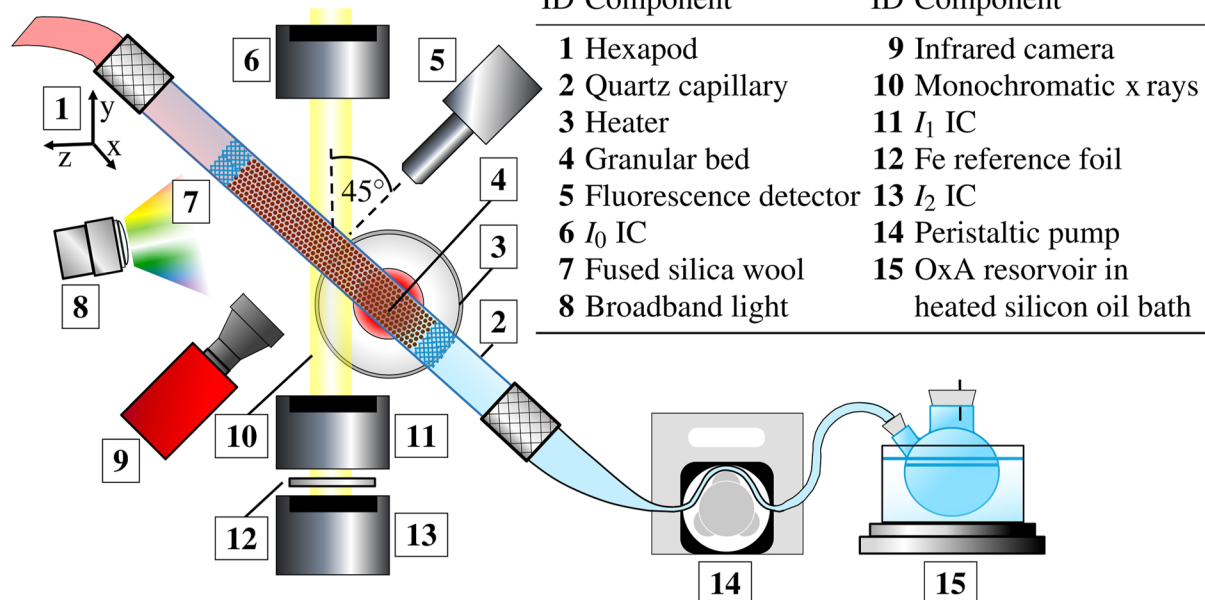


FIG. 1. Schematic drawing of the experimental setup. Broadband light was only supplied to a subset of the experiments.

The x-ray absorption is measured using the continuous scanning mode of the monochromator, and the energy range decreased compared to the dry reference scans to capture the physical phenomena during the dissolution experiments. The energy increment was set to 0.7 eV at the vicinity of the Fe K absorption edge and to 1.3 eV at the post-edge region; the measurement time per scan is 120 s. These scans are hereafter referred to as Quick-Scans (QS). After the preparation of the particles, a mass of 10 mg was filled into the quartz capillary (2) of 1 mm inner diameter and a wall thickness of 10 μm (WJM-Glas Müller GmbH). To prevent a sample displacement during the experiment, fused silica wool (7) was used at both ends of the formed particle bed. The capillary was then secured in a steel frame, sealed by an epoxy adhesive and tightly connected to the main flow circuit. If the particles were exposed to light during the experiment, a combined deuterium/halogen lamp (8) provided a broadband spectrum of 190–2500 nm (Ocean Optics, DH-2000-S-DUV) via a fiber-optic cable attached to the steel frame. The end of the cable was ~ 2 cm from the capillary. To prime the experiment, the OxA was conveyed from the heated reservoir (15) to the beginning of the capillary using a peristaltic pump (14, Ismatec, Reglo Digital). First, the flow was stopped before the OxA reached the particle bed, and immediately before the recording of the absorption spectra, the pump was started again to follow the wetting of the particle bed. It was observed as a discontinuous jump in the recorded absorption intensity after ~ 3 to 5 min, thus marking the beginning of the reaction. Once the OxA filled the measurement spot, the absorption of x rays at this energy range in the liquid medium was significant and the fluorescence mode had to be used for *in situ* measurements. After the spectra of one experiment have been successfully recorded, the capillary with its metal frame was removed, and the flow circuit was cleaned by alternately pumping air

and distilled water through the system. After the last cleaning cycle, a new metal frame with a capillary containing the next iron oxide sample is connected to the flow circuit. The duration of an experiment was set to a minimum time of 90 min. However, depending on factors such as signal-to-noise ratio, repetition of an experiment, and beam availability, some experiments have been conducted for a longer time.

C. Temperature evaluation

The temperature of the reactor was controlled both by pre-heating the OxA and by a gas blower heater (3) placed directly beneath the capillary and monitored by an infrared camera (9, InfraTec ImageIR 8300) focused on the particle bed inside the capillary. Due to parasitic heat fluxes along the fluid flow path, the gas blower was not heating adequately when set to the desired temperature of 60 $^{\circ}\text{C}$. To achieve ~ 60 $^{\circ}\text{C}$ mean reaction temperature, the gas blower temperature has to be set to 125 $^{\circ}\text{C}$ once the peristaltic pump had been started and the flow set to the minimal rate. Due to the flow of OxA, the position where the targeted temperature is reached was found to be shifted in the direction of the feed flow from the gas blower nozzle and the XAS measurements were conducted on this position [see Fig. 2(a)]. To avoid overshooting the target temperature, the gas blower setpoint was increased at a rate of 5 K/min starting from 50 $^{\circ}\text{C}$. However, the operation of the peristaltic pump with eight rollers results in a pulsation of the flow volume. Consequently, the heat transfer coefficient varies periodically over time with a period of ~ 21.1 s, thus leading to a periodic change in the thermal boundary layer thickness inside the capillary. The resulting temperature fluctuations, evaluated by an in-house MATLAB code, are shown in Fig. 2(b).

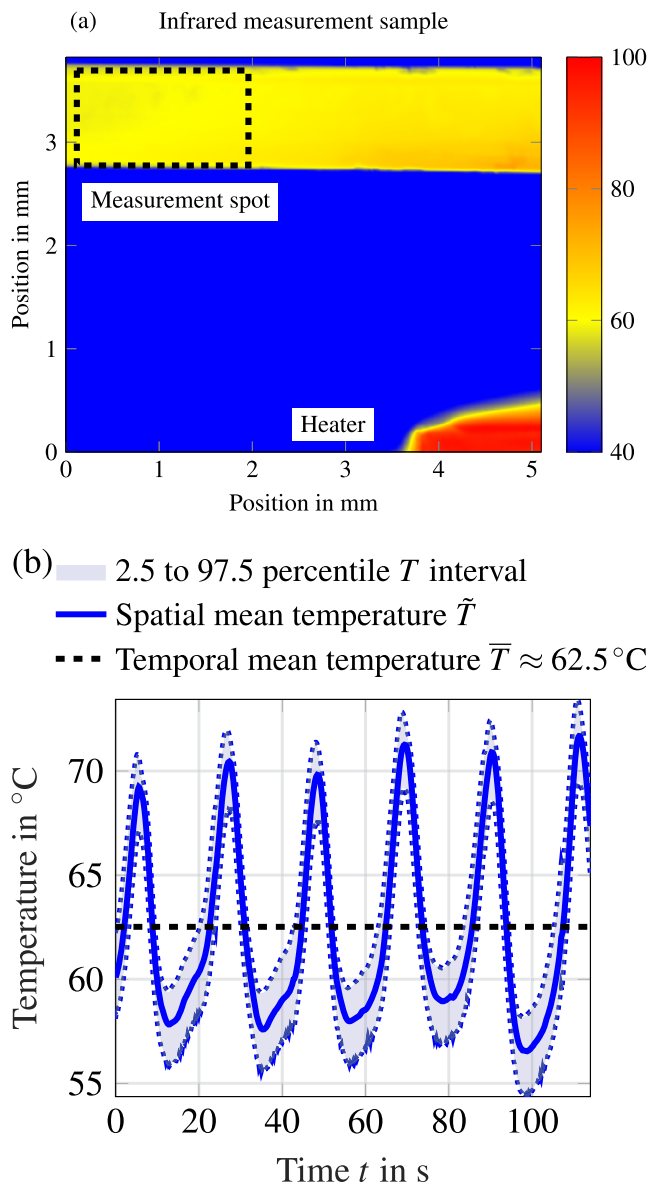


FIG. 2. (a) Example of an image captured by the infrared camera after the sample temperature has reached the stable state with the approximate position and size of the measurement spot of 143×72 pixels, corresponding to $\sim 1.9 \times 0.9$ mm². (b) Temperature evolution inside the measurement spot marked by the rectangle in (a). The shaded area gives the 95% range of temperatures at each captured image measured at 7 fps.

To determine the temperature variation inside the measurement spot, the interval is calculated in which 95% of all the temperatures are contained. As shown in Fig. 2(b), the minima of the temperature evolution are associated with a greater interval possibly due to the higher gradient in the vertical position at higher flow velocities. While these temporal and spatial temperature fluctuations introduce some uncertainty, the time scales of the processes are much longer than the periodic fluctuations, as shown in Sec. III.

Even for a quick energy scan (QS), there are between 5 and 6 temperature cycles completed, mitigating their influence on the collected spectra. The mean temperature across the displayed cycles is close to the target temperature of 60 °C at ~ 62.5 °C. X-ray diffraction (XRD) measurements were carried out at the Institute of Catalysis Research and Technology (KIT, Eggenstein-Leopoldshafen, Germany) using a X'Pert PRO machine (Malvern PANalytical). For the simulation of XRD patterns, the software Mercury v.3.5.1^{72,73} was used.

Fe-57 Mössbauer spectroscopy was carried out at room temperature in the Catalysts and Electrocatalysts group (TU, Darmstadt, Germany).

D. Spectroscopic data processing

The IFEFFIT software package⁷⁴ was used to calibrate the obtained Fe K spectra using the first inflection point of the Fe foil spectrum setting it to the tabulated value of 7112 eV. The spectra were then analyzed using a combination of the Python-based Larch software package (version 0.9.74)⁷⁵ and MATLAB. Using the Latrix application, normalization and background subtraction are performed by fitting a first-degree polynomial below the edge and a second-degree polynomial above the edge for the QS and third-degree polynomial for the LS. The normalized spectrum is obtained by the subtraction of the fitted polynomial below the edge from the spectrum and subsequently dividing the spectrum by the edge jump, determined as the absolute difference in absorption values $\mu(E)$ between the polynomial fits at the edge position. The edge position itself was determined based on the maximum of the first derivative of $\mu(E)$ ⁷⁶ using the Larch software.

Merging of the normalized spectra has been performed for experiments that have been measured using QS. In this case, eight spectra have been combined using the Larch software package to obtain a higher signal-to-noise ratio. If fewer than eight spectra remain at the end of the experiment, the final merge comprises the previous eight spectra and all remaining spectra. However, the merging causes temporal smoothing, which could potentially obscure fast effects. As shown in Sec. III, this only poses a challenge for the spinel-type oxides, where the rate of change in the spectra is highest in the beginning before monotonically approaching zero. Thus, in this case, the first eight spectra have been processed without merging.

The pre-edge in the recorded absorption spectra results from electronic transitions from the 1s core state to empty anti-bonded states of d-symmetry⁷⁷ that are sensitive to the oxidation state and coordination geometry.^{78,79} The pre-edge data processing in this article follows the procedures outlined in the literature,^{78,80–85} which first requires the approximation of the normalized edge-onset by some form of modeling function and subsequently subtracting the fit from the absorption data. The extracted pre-edge is then deconvoluted using standard functions. While these steps are consistent in the literature, there exist different approaches as to what modeling function to use for either edge-onset or pre-edge features. While Galois, Calas, and Arrio⁸¹ and Quartieri *et al.*⁸³ followed the procedure of Calas and Petiau⁸⁰ and used a regular arctangent, Simon *et al.*⁸⁴ and Wilke *et al.*⁸⁵ fitted a spline and Boubnov *et al.*⁷⁸ even concluded that a sum of an arctangent and a first-degree polynomial is best suited for approximating the edge-onset. For the pre-edge features, there exists a similar bandwidth of options; however, commonly used⁸⁶ are either Lorentzian, Gaussian, or a

pseudo-Voigt function, which is able to blend the latter two. In this study, we use the combination of a first-degree polynomial in combination with a Voigt function to approximate the background using the data several electron volts before and after the pre-edge feature (see Sec. III A), while the pre-edge features were fitted with two Gaussian functions, denoted $f_{g,1}$ and $f_{g,2}$. This configuration was chosen considering the results of Boubnov *et al.*,⁷⁸ who used two pseudo-Voigt functions for their standard resolution case with Gaussian fractions close to 100% for the reference oxides considered here.

Adhering to the procedures described in the literature,⁷¹ to obtain the Extended X-ray absorption Fine Structure (EXAFS) data, the background subtraction of the normalized LS (QS if different) spectra has been performed based on the AUTOBK algorithm⁸⁷ with a distance cutoff at 1 Å, using a k -weight equal to 2, setting no clamp restrictions (data appending to avoid overshoot) for the spline fit up to a maximum k -value of 12.5 Å⁻¹ (10.0 Å⁻¹). For the Fourier transform, FT, the k^2 -weighted data are prepared by a Hanning window function using a sill size equal to 1 Å⁻¹ in the k -range from 0.5 to 12.0 Å⁻¹ (0–8.0 Å⁻¹) to smooth the sudden truncation of $\mathcal{X}(k)$.

X-ray microcomputed tomography (μ -XCT) analysis was performed using a Zeiss Xradia Versa 520 X-ray microscope (Pleasanton, United States). The sample was filled in a capillary tube and scanned using a 20 \times objective lens in binning 2 mode with a tungsten x-ray source. The instrument was operated at 60 kV and 83 μ A, employing a low energy filter to optimize transmission and the signal to noise ratio. The chosen setting provided an optical magnification of 20.06 and a voxel size of 0.77 μ m. The sample was scanned within the entire range of 0°–360°, and 3001 images were acquired with an exposure time of 8 s per image, which resulted in a scanning time of \sim 8 h. Reconstructions were performed with a commercial software package (Zeiss XMReconstructor), which uses an algorithm based on standard filtered back-projection. Evaluation of the particle characteristics was performed using an in-house MATLAB script.

Low temperature Mössbauer spectrum was recorded in transmission mode using a ⁵⁷Co/Rh source in order to determine the exact composition of the commercial maghemite Fe₂O₃ particles. The measurement was performed at 5 K for 2 days with a velocity window of \pm 12 mm/s. After the measurement, the folding step and velocity calibration were completed by using the sextet lines of standard α -Fe (25 μ m). The Recoil software was used for the fitting procedure.⁸⁸

The laser diffraction particle size analysis was performed by Sympatec GmbH using the HELOS system after the dry dispersion using the RODOS system.

III. RESULTS AND DISCUSSION

Prior to the dissolution experiments, the iron oxidation state, crystalline structure, particle size, and morphology of the various reference oxides and CIPs are characterized. The overall aim is twofold: first, to validate the structure and oxidation state of the reference oxides, and second, to characterize the CIPs to elucidate their differing dissolution characteristics described in Sec. III B.

Since the objective of this study is to investigate the influence of crystal structure and oxidation state on dissolution mechanisms for both pure and mixed-phase iron oxides, a number of iron oxides were chosen for characterization. This includes pure Fe^{II} oxides in both rhombohedral (hematite) and spinel (maghemite) structures, particles containing a mix of hematite and maghemite, magnetite, and w \ddot{u} rzite. CIPs contain a mixture of α - and γ -phases and additionally include Fe^{II} and Fe⁰ species.

A. Particle characterization

The structures of the Fe₃O₄ and γ -Fe₂O₃ particles are confirmed by comparing XRD measurements with a simulated pattern based on tabulated crystalline structures (see Fig. 19 in Appendix A). The crystallite sizes of the particles are estimated using both the Scherrer equation⁸⁹ (SE) and Williamson–Hall

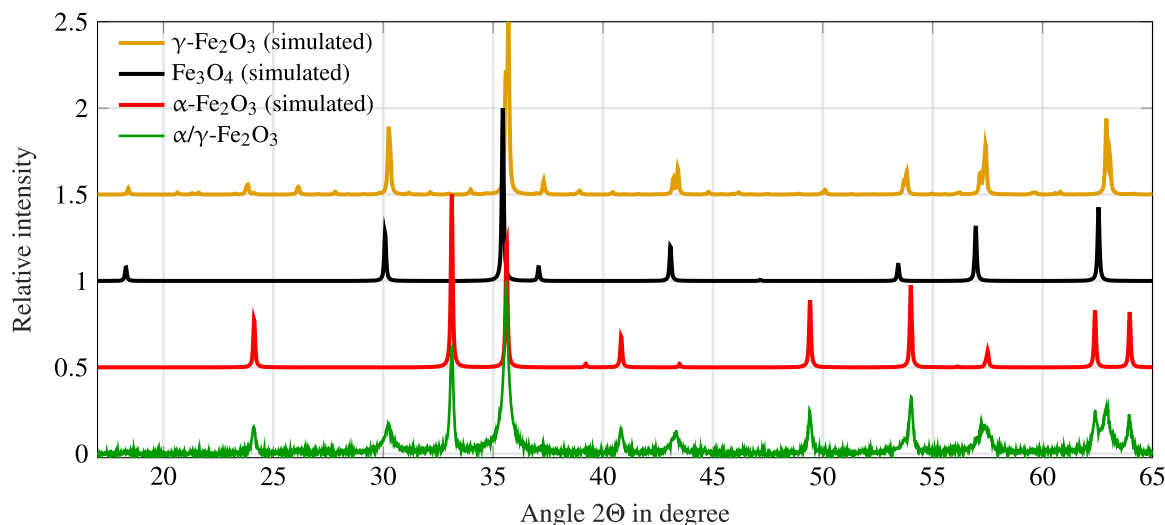


FIG. 3. XRD pattern of the mixed reference oxide; simulated data of iron oxides are scaled by their individual maximum. The intensity as a function of the angle 2Θ between the incident and diffracted beams is normalized to its individual maximum to enhance visibility.

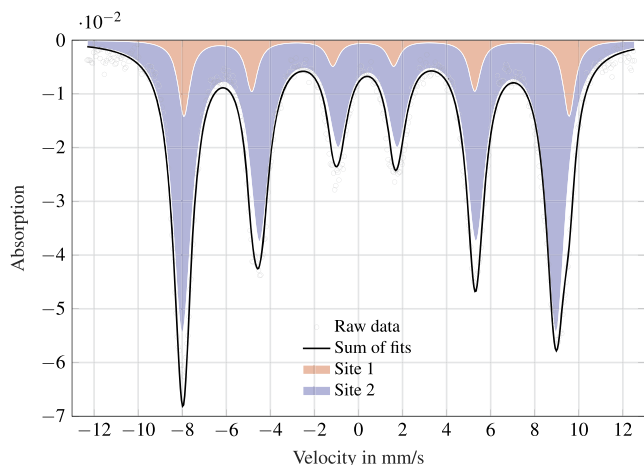


FIG. 4. Mössbauer spectrum (at 5 K) of the commercial maghemite powder (α/γ - Fe_2O_3), indicating the presence of maghemite (site 2) and hematite (site 1).

(WH) method,⁹⁰ employing an x-ray wavelength of 1.540 598 Å and assuming a shape factor $K = 0.9$. For the α - Fe_2O_3 particles, the crystallite size is determined as ~ 28.5 nm (WH) with a strain of -9.5×10^{-4} using the characteristic Bragg peaks at 24.1° , 33.1° , 49.4° , 62.4° , and 64° . Using the same peaks, the SE provided an estimate of 41.6 ± 6.6 nm, highlighting the significant influence of strain in the sample. The crystallite size of the magnetite sample is larger, ~ 71.3 nm (WH) with a strain of 1.3×10^{-3} , while the SE yielded 35.9 ± 5 nm using the Bragg peaks at 30.1° , 35.4° , 43.1° , 57° , and 62.6° . For the commercial maghemite Fe_2O_3 particles, the XRD data (Fig. 3) reveal an apparent mixture of the rhombohedral (α - Fe_2O_3) and spinel structures as in γ - Fe_2O_3 or Fe_3O_4 . By using only unambiguously assignable Bragg peaks for each phase, the crystallite size for the α -phase was

estimated to be 48.3 nm (WH), with a strain of 0.7×10^{-4} , using the peaks at 24.1° , 33.1° , 40.8° , 49.4° , and 63.9° . For the spinel phase, the WH method estimated the crystallite size at 21.8 nm, with a strain of 5.6×10^{-4} , based on peaks at 30.2° and 43.3° . The SE method produced the corresponding estimates of 46.7 ± 2.4 nm for the α -phase and 19.6 ± 0.5 nm for the spinel phase.

While the measured diffraction patterns align more closely with the theoretical predictions of γ - Fe_2O_3 than those of Fe_3O_4 , distinguishing between the two is challenging, as many of their characteristic peaks coincide (see Fig. 18 in Appendix A). To explore the structural differences in greater detail, Mössbauer spectroscopy is employed as a complementary technique⁹¹ to resolve hyperfine structures around the iron nucleus and determine its oxidation state^{92,93} even in amorphous structures, where XRD is less sensitive.⁹⁴ Low-temperature Mössbauer spectroscopy at 5 K is particularly effective for distinguishing between magnetite and maghemite, as ferric and ferrous ions share distinct hyperfine fields in the octahedron gaps of the spinel structure.⁹⁵ Figure 4 shows the recorded and subsequently fitted Mössbauer spectrum of the sample. As can be seen, two sextet sites can be obtained, in which sextet site 1 has a broader hyperfine field at 54.2 T, while the hyperfine field value of site 2 is at 52.6 T. As shown, for example, by Oh, Cook, and Townsend,⁹⁶ the larger magnetic hyperfine field of hematite (around 54 T) indicates the antiferromagnetic state of hematite, compared to γ - Fe_2O_3 , which exhibits a hyperfine field around 52 T. Hence, it is evident that the sample contains α - Fe_2O_3 (14%) and γ - Fe_2O_3 (86%). Magnetite can be excluded, as lower magnetic fields in combination with center shifts above 0.5 mm/s would have been expected.⁹⁷

The diffraction pattern of the CIPs shows similar features to those reported by Buchheiser *et al.*,⁶⁴ indicating a mixture primarily of α - Fe_2O_3 and Fe_3O_4 , with traces of FeO and α -Fe, as shown in Fig. 5(a). While the characteristic Bragg peaks of α - Fe_2O_3 , Fe_3O_4 , and α -Fe (with α -Fe observed at $2\theta \approx 44.7^\circ$, according to Buchheiser *et al.*⁶⁴) closely match theoretical predictions, the

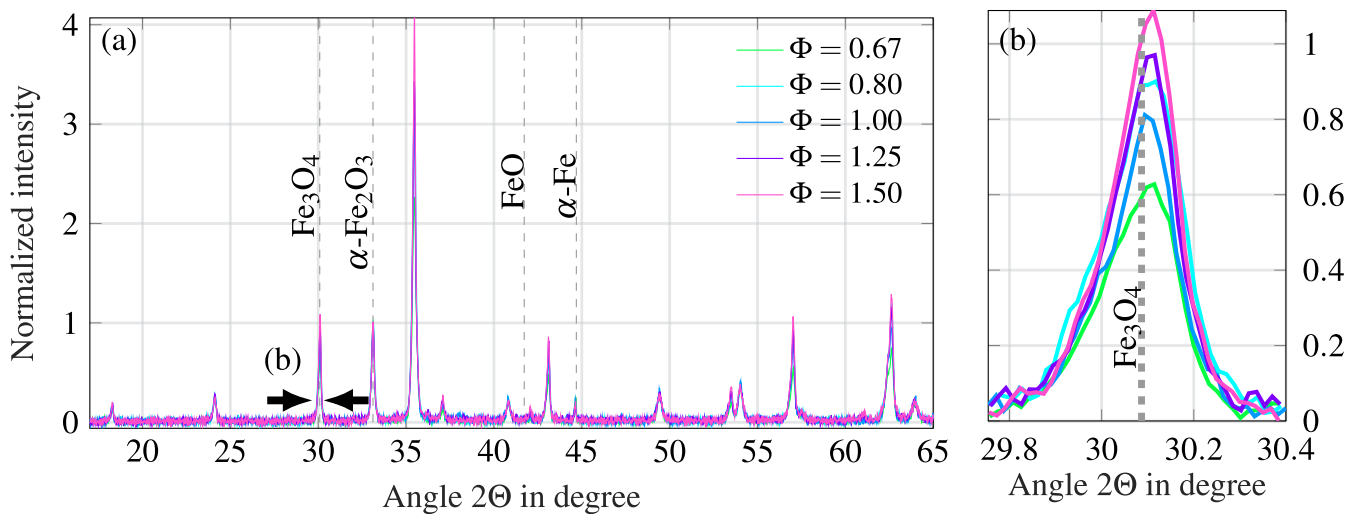


FIG. 5. (a) XRD patterns of the Combusted Iron Particles (CIPs); the characteristic angles for each reference oxide are marked with vertical dashed lines. (b) Detail of the characteristic magnetite peak at $2\theta \approx 30.1^\circ$.

Bragg peak associated with FeO at 41.7° does not align with the observed CIP peak, which is centered around 43.1° . Nevertheless, the presence of FeO is consistent with findings from Choisez *et al.*,⁶⁵ where particles that failed to ignite were found to contain Fe, FeO, and Fe₃O₄ during their oxidation in preheated air, while combusted particles of ~ 40 μm diameter were composed of α -Fe₂O₃ and Fe₃O₄. To estimate the mean crystallite size of hematite and magnetite in the sample, the unambiguously assignable peaks at 24.1° , 33.1° , 40.8° , 49.4° , 54° , and 64° (α -Fe₂O₃) and 18.3° , 30.1° , 53.5° , and 57° (Fe₃O₄) are used. While the WH method was applicable for the pure iron oxides, the CIPs showed significant scatter in the α -phase, likely due to the presence of amorphous components. Therefore, only the more robust SE was applied, yielding α -Fe₂O₃ crystallite sizes of 36.5 ± 7.6 , 32.3 ± 6.4 , 39.1 ± 6.6 , 34.2 ± 10.4 , and 33.1 ± 9.4 nm for increasing Φ . In general, the crystallite size of Fe₃O₄ was estimated slightly greater than α -Fe₂O₃ with values of 39.2 ± 6.1 , 39.5 ± 2.2 , 43.8 ± 5.0 , 43.1 ± 6.1 , and 47.2 ± 7.9 nm. However, in both cases, there is no significant influence of Φ on the crystallite size.

Furthermore, consistent with the literature, increasing the fuel-to-air equivalence ratio (Φ) leads to a reduction in Fe₃O₄ content in the particles. To assess this, the Bragg peak of α -Fe₂O₃ at $2\theta \approx 33.1^\circ$ is used as a reference and fitted with a Voigt function for each CIP. The diffraction patterns are then normalized by the intensity of this peak, allowing for a comparison of the relative intensities of the peak associated with Fe₃O₄ at $2\theta \approx 30.1^\circ$. As shown in Fig. 5(b), the magnetite content generally matches expectations based on the fuel-to-air equivalence ratio. However, the $\Phi = 0.8$ CIPs deviate from this trend, exhibiting a higher magnetite content than anticipated.

Since the degree of iron oxidation is influenced not only by the fuel-to-air ratio during combustion but also by the particle size,⁶⁴ quantitatively analyzing the XRD data becomes challenging. Both the size and phase of the particles affect the characteristics of the diffraction peaks. The CIPs used in this study exhibit a non-normal size distribution with a heavy right tail,⁶⁴ and the magnetite content generally increases with particle size. Thus, the observed deviation in the $\Phi = 0.8$ CIPs may stem from a non-representative sampling of larger particles for XRD analysis.

Interestingly, although both α/γ -Fe₂O₃ and combusted iron particles contain α - and γ -phases, their diffraction patterns differ. This variation could be attributed to the higher diversity of Fe oxide species and differences in the internal crystal structure of the CIPs, as highlighted by Choisez *et al.*⁶⁵

The phase composition of the CIPs can be derived from the analysis of the pre-edge and near-edge features of the XAS spectra (Fig. 6) providing detailed insights into the average coordination geometry and oxidation state of the particles.^{79,85,98} The high centrosymmetry of the octahedral coordination in FeO and the rhombohedral crystalline structure of α -Fe₂O₃ result in allowed quadrupolar transitions, translating into a less intense pre-edge, as observed in Fig. 6(b). Consequently, if a process causes atoms in the crystal structure to be displaced from their initial centrosymmetric positions, introducing structural disorder and overlap of atomic orbitals that increase the probability of electron transitions, the intensity of the pre-edge peak may increase.^{99,100} For example, Vitova *et al.*¹⁰¹ demonstrated through FEFF calculations that the pre-edge intensity of lithium niobate increases with the increasing presence of vacancies in the crystal structure, whether from the removal of lithium or oxygen atoms. In terms of crystal

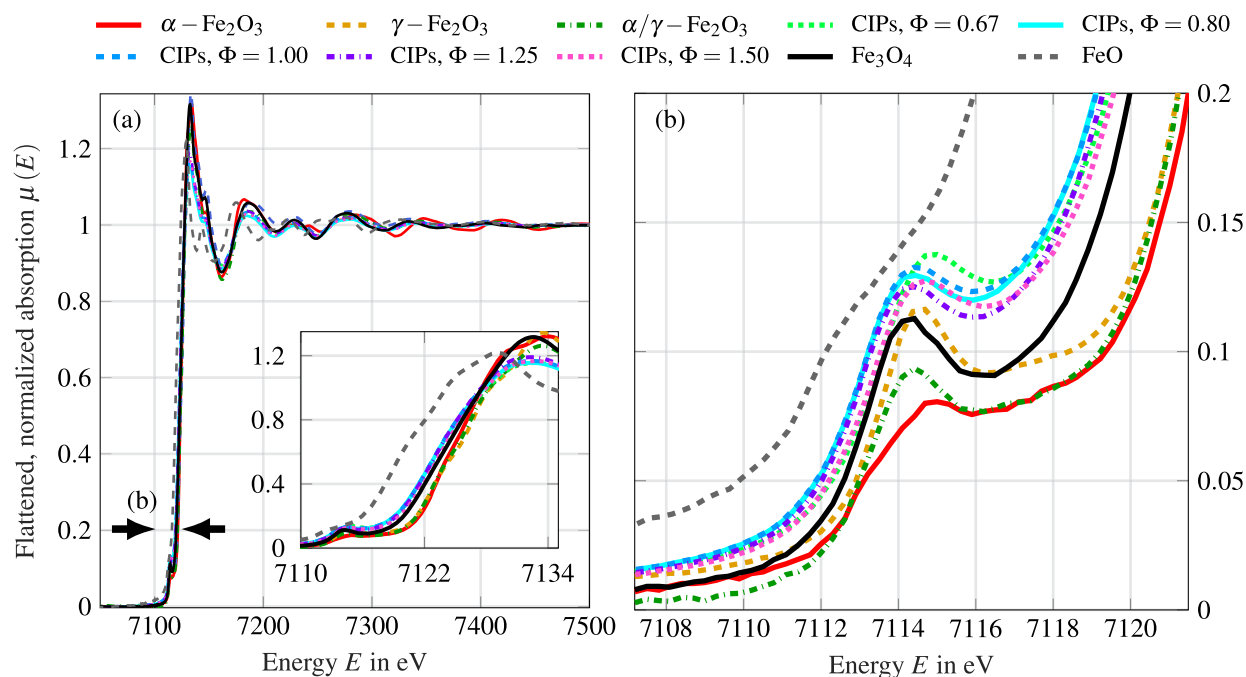


FIG. 6. (a) Fe K XAS spectra of the combusted iron particles (CIPs) for varying fuel-to-air equivalence ratio Φ in comparison with reference oxides, all recorded in transmission mode. The inset displays the XANES region in detail. (b) Pre-edge features of the scans presented in (a).

restructuring, the simulated pre-edge intensity generally increased with the increasing displacement of the Nb absorber. However, there was one direction of displacement that actually caused a decrease in intensity, even though the displacement caused a higher centrosymmetry of the structure, highlighting the complexity of interpreting pre-edge features. For the other oxides shown in Fig. 6(b), a distinctive peak characteristic of the spinel crystal structure,⁷⁸ which contains tetrahedral components, can be observed.

Based on these fingerprint features of standard iron oxides, the coordination structure of the CIPs can be evaluated. Consistent with the Mössbauer and XRD results, the peak is more pronounced for γ -Fe₂O₃ and Fe₃O₄, indicating a higher proportion of the γ -phase with increased Φ . Conversely, α/γ -Fe₂O₃ and the CIPs display a notable similarity in their less intense peak shape and prominence, despite their differences in the internal structure, as revealed by Mössbauer spectroscopy and XRD. The absorption intensity [$\mu(E)$] at $E = [7114, 7115]$ eV is higher for the CIPs, which could point to a higher metal-ligand covalency, which in turn promotes more intense p-d orbital mixing for non-centrosymmetric structures. The intensity is also influenced by the oxidation state as it dictates the number of unoccupied d-orbitals available for the $1s \rightarrow 3d$ transition.

To analyze both coordination and oxidation state, the pre-edge is examined for the enclosed area and its energy position, as outlined in the literature.^{78,79,84} The enclosed area is determined by fitting the pre-edge following the procedure described in Sec. II D and summing the integrals of the two Gaussian functions. The energy position, indicative of the formal oxidation state, is calculated as the area-weighted Gaussian centroids. An example fit with its residual is shown in Fig. 7(a); other fits are shown in Figs. 20 and 21 in Appendix A. The resulting variogram containing all fits is shown in Fig. 7(b), where the error bars represent the standard deviation obtained from the fitting procedure.

As shown in Fig. 7(b), the oxides cluster according to their phase and oxidation state: particles with higher Fe^{III} are located at higher energies, while particles with greater centrosymmetry exhibit a lower intensity. As evident in Figs. 6 and 7(b), the CIPs are almost indistinguishable regarding their centroid position and intensity, close to Fe₃O₄. An exception are the $\Phi = 0.67$ CIPs, which, consistent with the XRD analysis, display the highest Fe^{III} content. While from Fig. 6(b), a centroid position for $\Phi = 1.5$ is expected to be closer to that of $\Phi = 0.67$, the analysis of pre-edge revealed the relatively high uncertainty for $\Phi = 1.5$ compared to the other CIPs [see Fig. 7(b)]. One contributing factor to the minor spectral differences observed among the CIPs could be a systematic bias during particle preparation, which may favor smaller particles during dilution with cellulose or fused silica, as described in Sec. II B. Particularly in the case of sieving, larger particles would be less likely to pass through the 200 μm sieve, as reaching the critical particle size would result in less mass adhering to the fused silica. Since smaller particles exhibit a higher degree of oxidation,⁶⁴ this could reduce the observed effect of Φ on the particle oxidation state. Another methodological factor could be the interaction between the particle and the x-ray beam: The absorption cross sections of Fe₂O₃ and Fe₃O₄ at 7150 eV are estimated through the interpolation of a second-order

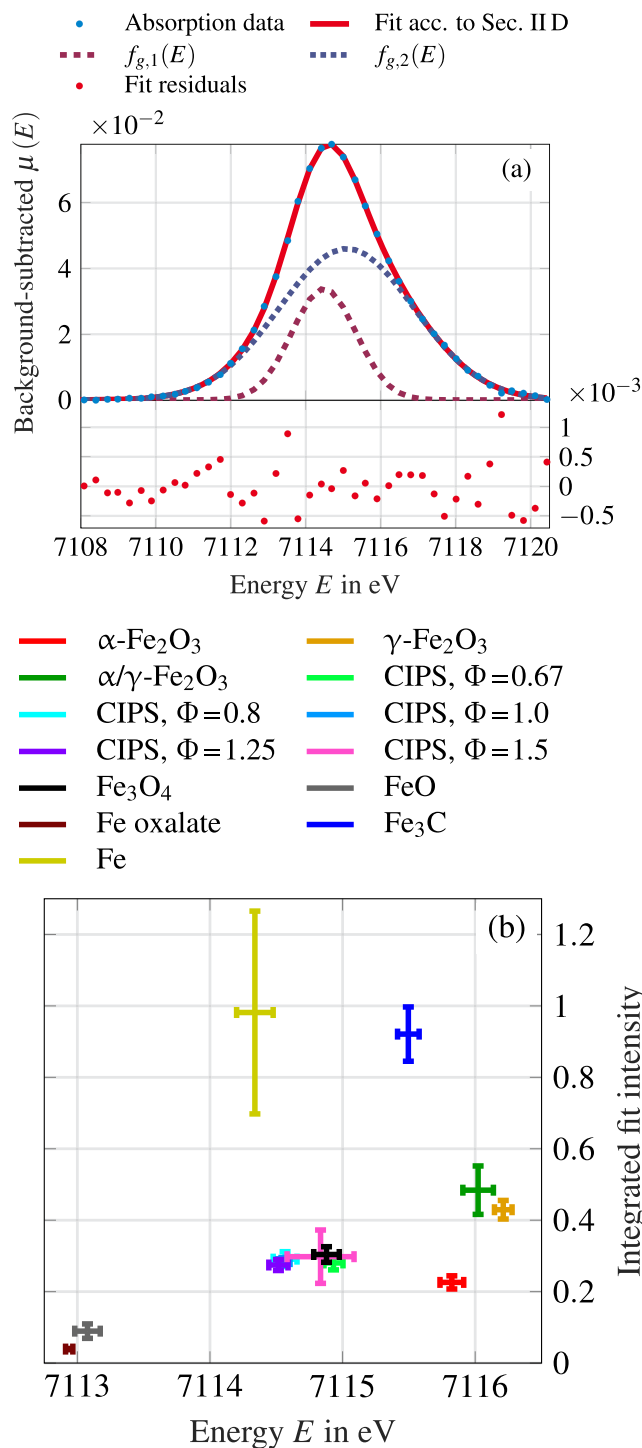


FIG. 7. (a) Fe K pre-edge fit for $\Phi = 1.5$ CIPs. (b) Variogram comprising the centroid position and the total area of pre-edge for reference oxides and CIPs shown in Fig. 6.

polynomial fit to tabulated values^{102,103} to be ~ 293 and $303 \text{ cm}^2/\text{g}$, respectively. With average bulk densities of 5.26 and 5.18 g/cm^3 ,¹⁰⁴ this results in nearly equal sample thicknesses of $\sim 13.0 \mu\text{m}$ (Fe_2O_3) and $12.7 \mu\text{m}$ (Fe_3O_4) for a desired minimum $\mu(7150 \text{ eV}) = 2$. As a result, the signal measured in I_1 would be biased toward smaller particles, since larger particles would attenuate the signal beyond the detection limit. If the CIPs possess a core-shell structure with an $\alpha\text{-Fe}_2\text{O}_3$ shell and an Fe_3O_4 core containing $\alpha\text{-Fe}_2\text{O}_3$ interstitials, as described by Choisez *et al.*,⁶⁵ this could bias the measurements toward $\alpha\text{-Fe}_2\text{O}_3$ even when using the fluorescence mode. The higher frequency of micro-explosions in oxygen-rich combustion environments, which produces a greater number of smaller particles, may also contribute to the elevated Fe^{III} content observed in $\Phi = 0.67$. While the particle-size-dependent attenuation effect also affects the reference oxides, it is less pronounced because their median particle size is significantly smaller and there is no structural variation across the particle volume.

Information about the structure surrounding the Fe absorber can also be extracted from the EXAFS oscillations $\mathcal{X}(E)$, processed as described in Sec. II D (see Fig. 22 in Appendix A). The magnitude of the Fourier transform, FT, enables the evaluation of frequencies present in $\mathcal{X}(k)$ as a function of the apparent distance R , as shown in Fig. 8. The peaks represent the combined backscattering contributions of neighboring atoms, based on their atomic species and structural arrangement within the particles. The EXAFS data for the pure and mixed-phase oxides corroborate the XRD results of the corresponding standard crystalline structures. Compared to the iron oxide references, the amplitude of both the first and second coordination shells in the CIPs is lower, likely due to increased disorder in their crystalline structure. Although the EXAFS data of

the CIPs exhibit similar features, there are notable differences, such as the shape of the peak in the first coordination shell of the $\Phi = 0.67$ CIPs. The feature at $\sim 1 \text{ \AA}$ seems to stem from a superposition of two peaks for the $\Phi = 0.67$ CIPs, similar to most of the displayed oxide references. When rescaled by their maximum, the first coordination shell of $\Phi = 0.67$ CIPs and $\alpha\text{-Fe}_2\text{O}_3$ almost perfectly overlap (see Fig. 24 in Appendix A), indicating a higher hematite content in the particles, as observed in the XRD data and from the pre-edge analysis. Notably, the second coordination shell distance R of the CIPs at $\sim 2.6 \text{ \AA}$, associated with the Fe-O-Fe interaction, is closer to the $\alpha\text{-Fe}_2\text{O}_3$ position rather than Fe_3O_4 . This conformity is in contrast to the characteristic hematite peak at $\sim 3.1 \text{ \AA}$, which is greatly suppressed for the CIPs. Rescaling the EXAFS by their FT maximum reveals that the decreasing magnitude of this feature correlates with an increasing γ -phase content in the CIPs. Besides the nominal oxidation state, distinguishing between Fe_3O_4 and $\gamma\text{-Fe}_2\text{O}_3$ remains challenging, as both share most spectral features.¹⁰⁵ In general, the EXAFS features of the CIPs' second coordination shell bear a close resemblance to those of the $\alpha/\gamma\text{-Fe}_2\text{O}_3$ particles, with a lower amplitude, including the peak at $\sim 3.6 \text{ \AA}$, which is absent for both Fe_3O_4 and $\gamma\text{-Fe}_2\text{O}_3$. This can be explained by the shared structural composition of both the α - and γ -phases, but is surprising given the structured layout of the CIPs. EXAFS studies of other layered iron oxide particles in the literature predominantly focus on nanoparticles,¹⁰⁶⁻¹⁰⁸ and it has been demonstrated that multiphase composites may not simply behave like a superposition of bulk materials, as detailed by Kuzmin and Chaboy.¹⁰⁹ In particular, size-dependent effects have been observed in magnetite nanoparticles, which could only be detected in the XANES characteristics of single-phase, nonstoichiometric oxides.¹¹⁰

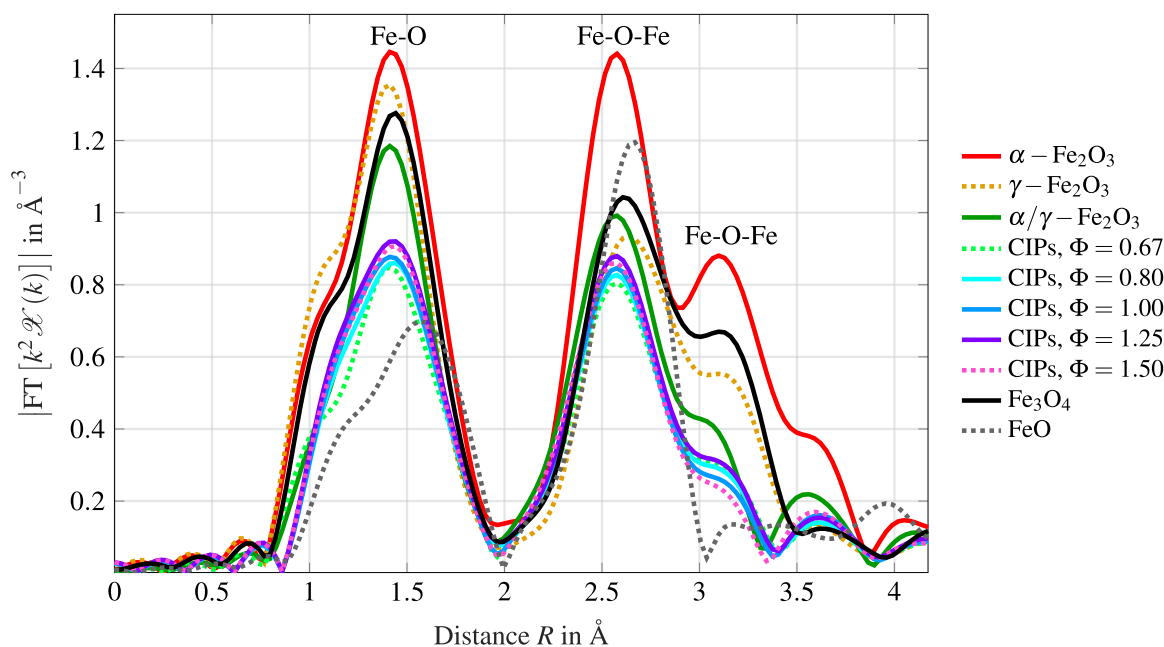


FIG. 8. Fourier transformed (k^2 -weighted) EXAFS data at the Fe K-edge of the CIPs for varying fuel-to-air equivalence ratio Φ in comparison with reference oxides, all recorded in transmission mode (not corrected for phase shift).

Besides the phase composition and oxidation state of the particles, their size distribution and morphology are essential. The size distribution of the CIPs has already been reported by Buchheiser *et al.*⁶⁴ with median particle sizes increasing from 7.84 μm at $\Phi = 0.67$ to 9.78 μm at $\Phi = 1.5$ due to a higher frequency of micro-explosions in oxygen-rich mixtures. As shown in Figs. 9(a)–9(d), the pure and mixed-phase oxides $\alpha\text{-Fe}_2\text{O}_3$, $\gamma\text{-Fe}_2\text{O}_3$, $\alpha/\gamma\text{-Fe}_2\text{O}_3$, and Fe_3O_4 all exhibit a variety of shapes with rough surfaces. Notably, Fe_3O_4 are on average smaller than their pure counterparts and CIPs. The polydispersity apparent in the SEM images is subsequently quantified by laser diffraction particle size analysis, yielding mostly bimodal distributions (see Fig. 28) with a median particle diameter of ~ 11.2 μm ($\alpha\text{-Fe}_2\text{O}_3$), 32.9 μm ($\gamma\text{-Fe}_2\text{O}_3$), 9.1 μm ($\alpha/\gamma\text{-Fe}_2\text{O}_3$), and 0.9 μm (Fe_3O_4). While the values allow for a comparison between the reference oxides, they should be interpreted with caution due to the highly non-convex form and pronounced surface roughness of the particles. These characteristics can pose significant challenges for particle size analysis using diffraction-based methods.^{111,112} The size distribution and particle shape can be further analyzed using x-ray microtomography (μCT) for particles with a volume-equivalent diameter greater than 3.5 μm . This analysis has been conducted for the CIPs at $\Phi = 0.67$ and $\Phi = 1.5$, as well as for the $\alpha/\gamma\text{-Fe}_2\text{O}_3$ particles, as shown in Fig. 9(c). For the $\alpha/\gamma\text{-Fe}_2\text{O}_3$ particles, an equivalent spherical median diameter of 4.39 μm was calculated, with a 95% confidence interval of [4.37, 4.40] μm , obtained through a bootstrapping procedure.

As shown in Fig. 9(e), the majority of CIPs are spherical, regardless of their size. Particles exceeding 10 μm sometimes exhibit cracks and grooves across the surface, as reported in the literature.^{65,113–115} In very rare cases, non-spherical particles can be observed, as illustrated in Fig. 9(f). This was the only particle of all CIP SEM images as shown in Fig. 27. These particles fit the description of uncombusted particles as shown in detail by Choisez *et al.*⁶⁵ In the μCT images (Fig. 10), the hollow structure of the bigger particles becomes apparent.

X-ray tomograms (μCT , Fig. 10) reveal that there are several particles of different size with cavities in their core, as previously reported in the literature.^{65,113–115} According to Choisez *et al.*,⁶⁵ these cavities are filled with oxygen generated during the combustion process. Consistent with the findings of Choisez *et al.*,⁶⁵ particles that showed signs of internal fracture may subsequently accumulate smaller particles in the cavities during transport and storage. An example is highlighted in Fig. 10(a) (circle 1). While some particles have spheroidal cavities, their internal structure is more complex. For larger particles, the 3D reconstruction reveals a network of interconnected voids extending through the particle, as illustrated in Fig. 11(a). Since brighter spots in the 2D scan in Fig. 10 mark higher iron concentrations, information on global and local iron content can be obtained in addition to the general shape and size of the particles. Consistent with reports from Buchheiser *et al.*,⁶⁴ the average volume content of iron increases with increasing Φ , since for $\Phi > 1$, there is more iron available than for complete oxidation to Fe_2O_3 . However, evaluation of the μCT scans yields

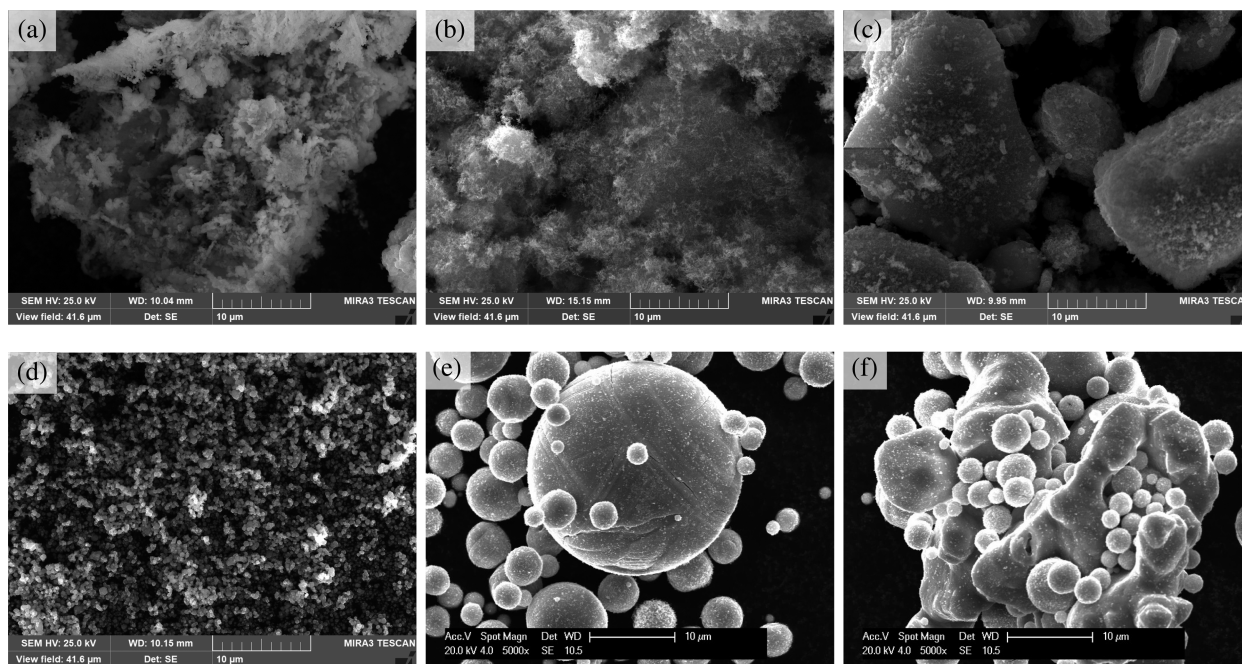


FIG. 9. Scanning Electron Microscopy (SEM) images of (a) $\alpha\text{-Fe}_2\text{O}_3$, (b) $\gamma\text{-Fe}_2\text{O}_3$, (c) $\alpha/\gamma\text{-Fe}_2\text{O}_3$, (d) Fe_3O_4 , and (e) combusted and (f) uncombusted particles at $\Phi = 0.67$. The scale bar indicates a length of 10 μm .

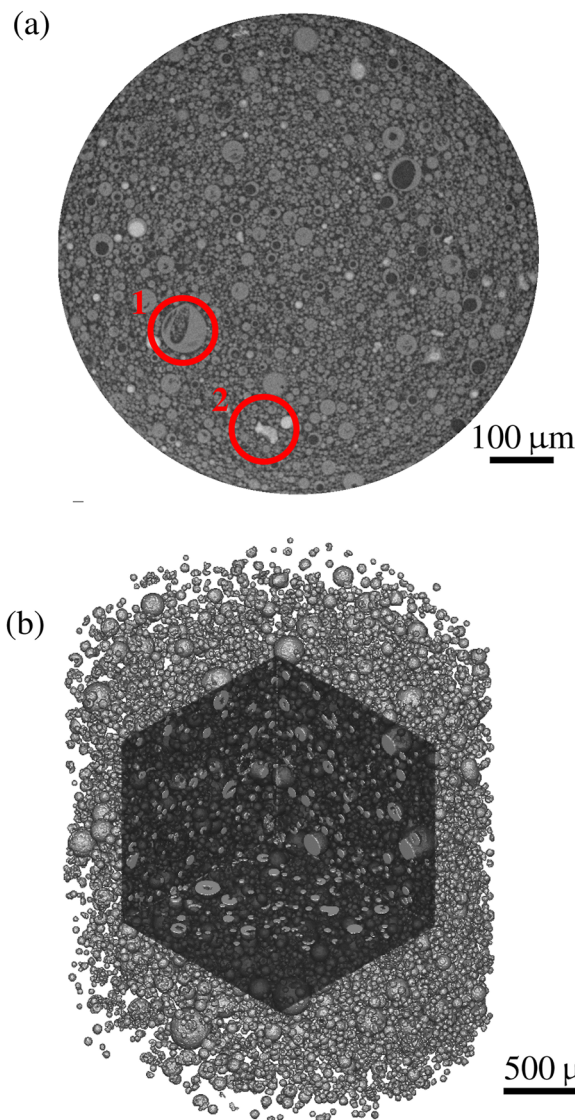


FIG. 10. μ CT measurements on $\Phi = 1.5$ CIPs. (a) Reconstructed 2D slice; the circle marked with 1 is the ruptured particle subsequently filled with smaller CIPs and the circle marked with 2 is the uncombusted iron particle. (b) Reconstructed 3D image; in rectangle cut-out, the 3D structure of the particles including cavities across different particle sizes can be seen.

higher average iron volume fraction, ranging from about 2% at $\Phi = 0.67$ to about 8% at $\Phi = 1.5$. This discrepancy may arise from the limitations of μ CT evaluation, which excludes particles smaller than a $6.9 \mu\text{m}$ volume-equivalent diameter, but which have a higher degree of oxidation.⁶⁴

Inspection of the distribution of iron within the oxide particles shows that, in addition to partially oxidized particles with an uncombusted iron core, spherical particles can also contain pure iron within their structure. Particles with a high iron content, as illustrated in Fig. 11(b), can exhibit highly non-spherical shapes as

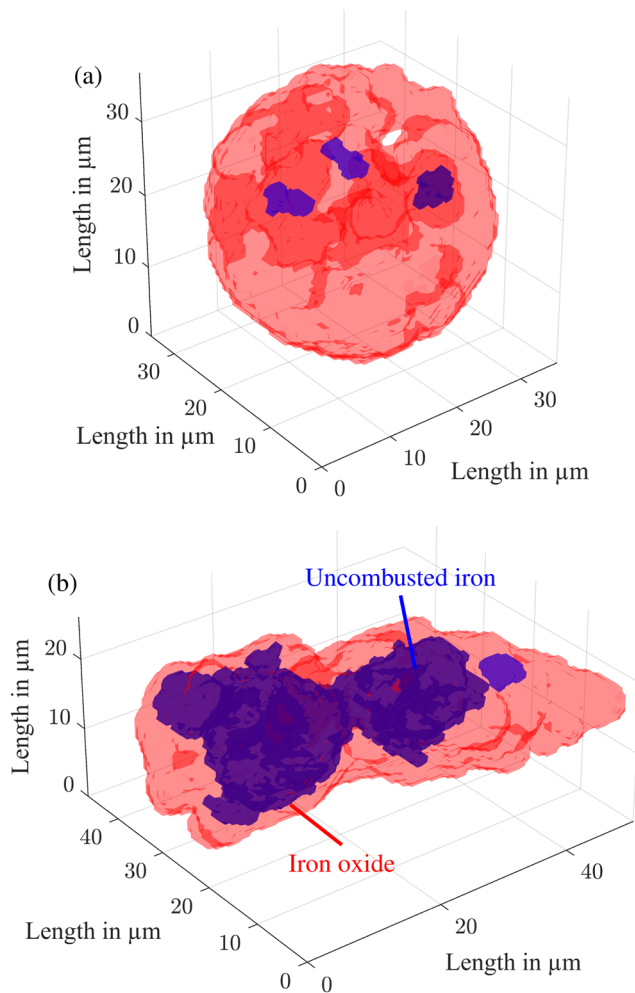


FIG. 11. Reconstructed 3D μ CT images of selected CIPs at $\Phi = 1.5$. (a) Particle of $\sim 25.7 \mu\text{m}$ volume-equivalent diameter with an uncombusted iron volume fraction of $\sim 0.7\%$. (b) Partially uncombusted, non-spherical particle of $\sim 25.33 \mu\text{m}$ volume-equivalent diameter with an uncombusted iron volume fraction of $\sim 35.7\%$. Red marked area—iron oxide, blue marked area—metallic iron.

also shown in Fig. 10(a) in the circle marked by 2 and Fig. 9(f). For almost all particles evaluated, the location of the uncombusted iron is close to the centroid of the whole particle.

The equivalent spherical median particle diameter for the sample volume shown in Fig. 10(b) was found to increase from $9.53 \mu\text{m}$ [(9.46, 9.59) μm bootstrapped 95% confidence interval] at $\Phi = 0.67$ – $9.71 \mu\text{m}$ [(9.65, 9.76) μm bootstrapped 95% confidence interval] at $\Phi = 1.5$. This is in agreement with the reports of Buchheiser *et al.*,⁶⁴ who attribute this evolution to the higher frequency of micro-explosions at lower Φ , which outweighs the increasing fraction of hematite and thus increasing fraction of oxygen per mole of iron with decreasing Φ . In summary, the size of the pure oxides particles is of similar range, yet considerably smaller than the CIPs. An exception are the Fe_3O_4 particles.

B. Dissolution experiments

The dissolution experiments described in this section initially explore the dissolution of pure α -phase particles, focusing on the mechanisms involved and the origin of humboldtine. This study then shifts to mixed-phase particles, specifically those with α - and γ -phases, which are similar to CIPs in the bulk, yet distinct in their structure and unaffected by the oxidation state as pure Fe^{III} . Following this, the dissolution of full spinel oxides (pure γ -phase) is examined, uncovering the unexpected formation of an amorphous structure instead of regular humboldtine crystals, and demonstrating no significant difference between maghemite and magnetite in the dissolution behavior. Finally, these insights are applied to CIPs, comprising mostly hematite and magnetite.

In all the dissolution experiments conducted in this study, the fluorescence signal consistently decreased as the oxides dissolved, with solubilized iron being transported out of the capillary (see Figs. 29–31 in Appendix B). The dissolution of $\alpha\text{-Fe}_2\text{O}_3$, $\alpha/\gamma\text{-Fe}_2\text{O}_3$, CIPs, $\Phi = 0.67$, and Fe_3O_4 was recorded two times each. While all the repeated experiments reproduced the spectral evolution features that distinguish the different oxides, the absolute value of $\mu(E)$ did not align with the first repetition in most cases at the same reaction time. This phenomenon was observed for all iron oxides except $\alpha\text{-Fe}_2\text{O}_3$ (see Figs. 33–40 in Appendix B). Considering the particle size distribution and the sample preparation method, which results in ~ 0.5 mg of iron oxide in the capillary, we attribute this discrepancy to variations in particle sizes within the measurement spot.

1. Dissolution of pure and mixed phase iron oxides

Shifts in the Fe K-edge toward lower energy positions are indicative of a reduction of the iron. As shown in Fig. 12, despite the decrease in fluorescence signal intensity (Fig. 29), the normalized spectra of the $\alpha\text{-Fe}_2\text{O}_3$ particles remain unchanged in both the pre-edge and XANES energy ranges. This stability suggests that the

reaction for this iron phase proceeds via the non-reductive pathway. In Figs. 12–17, the values denoted by \bar{t}_m represent the mean reaction time obtained from the merge (index m) of the spectra, as described in Sec. II D. The duration of each scan and merged scan is indicated by the color bar on the right, with white spaces representing dead time due to the reset of the double-crystal Si (111) monochromator position between scans. During these intervals, no spectral data were recorded.

Since absorption spectra in the pre-edge range are sensitive to the oxidation state and coordination geometry,^{78,79} the lack of spectral changes implies that the dissolution proceeds homogeneously across the crystal. This contrasts with the findings of preferential dissolution directions across the crystal, as described in Sec. I. One possible explanation is the size of the particles $\alpha/\gamma\text{-Fe}_2\text{O}_3$, where the change in coordination geometry on the surface is too small relative to the volume scanned, which includes the unexposed inner part of the particles. The stable oxidation state of the hematite particles during dissolution contrasts with the batch experiments by Taxiarchou *et al.*²² and Santawaja *et al.*,⁴⁰ where a build-up of ferrous iron was observed. This suggests that the presence of ferric iron complexes in the surrounding liquid may be necessary for the reductive pathway to occur. The purely non-reductive dissolution observed in this study contrasts with the findings of Vehmaanperä *et al.*,³⁹ whose DFT calculations on the dissolution of hematite by OxA predict the inherent formation of humboldtine, accompanied by iron reduction. This discrepancy may be attributed to the detection limits of the equipment used and differences in experimental boundary conditions, such as the higher OxA concentration and reaction temperature employed in this study. Increasing these boundary conditions shifts the reaction mechanism toward a non-reductive pathway, as discussed in Sec. I. In addition, the constant transport of reaction products away from the site may prevent the stable formation of humboldtine aggregates on the particle surface. Another possible explanation is the exclusion of light interactions and solution complexes from the theoretical

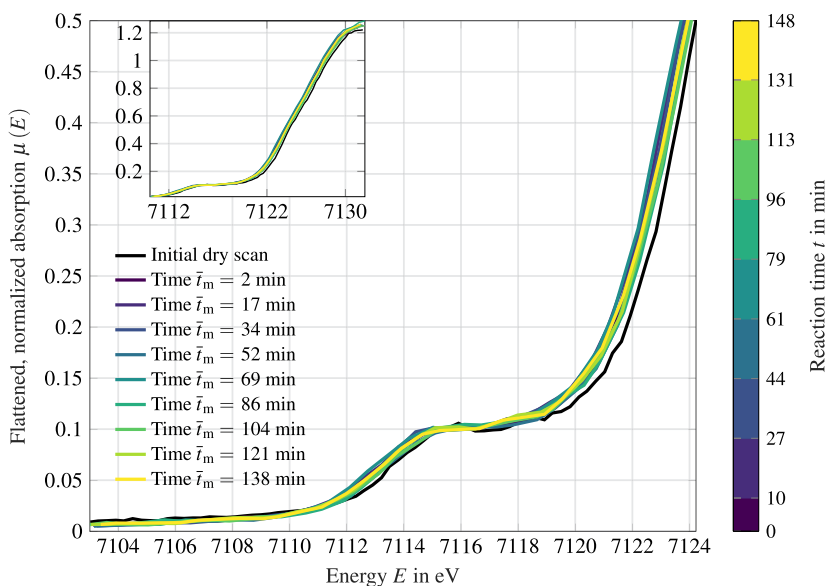


FIG. 12. Evolution of the pre-edge of Fe K XAS of the $\alpha\text{-Fe}_2\text{O}_3$ particles during dissolution without light, all recorded in fluorescence mode. The inset displays the XANES evolution in detail.

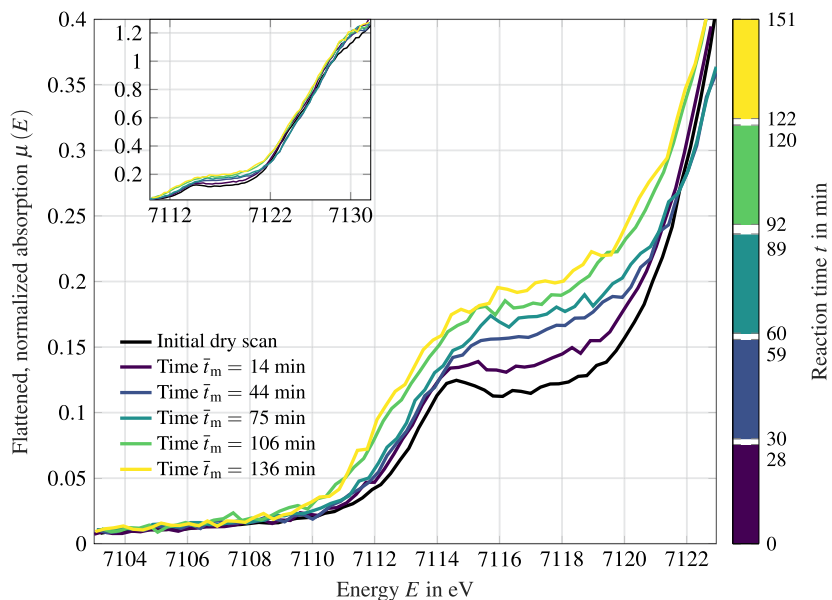


FIG. 13. Evolution of the pre-edge of Fe K XAS of the α/γ - Fe_2O_3 particles during dissolution without light, fluorescence mode. The inset displays the XANES evolution in detail.

simulations, as well as uncertainties regarding the initial form of oxalate attachment on the surface.⁵⁵ It is known that both light and the nature of surface complexes influence reaction mechanisms,^{21,23,116} and as Duckworth and Martin¹¹⁷ demonstrated, at higher pH (around 5), the surface complex formed with OxA is mononuclear and bidentate, with both oxygen atoms of the carboxyl group binding to one Fe atom on the crystal surface. The validation experiments in the study of Vehmaanperä *et al.*³⁹ were likely conducted using the setup of Salmimies, Vehmaanperä, and

Häkkinen,¹¹⁸ which involved exposure to light over several weeks, allowing a high degree of interaction, which contrasts with the experimental setup of the present study. Even under non-sinking conditions, Santawaja *et al.*³⁷ reported no precipitation over a range of iron oxide (0.05–1.3 mol_{Fe}/l) and OxA (0.1–1 mol/l) concentrations at an elevated temperature of 90 °C, crucially conducted in a light-shielded environment. Considering these results and the spectroscopic findings (Fig. 12) presented here, it seems that humboldtine formation is in fact not an inevitable step in the

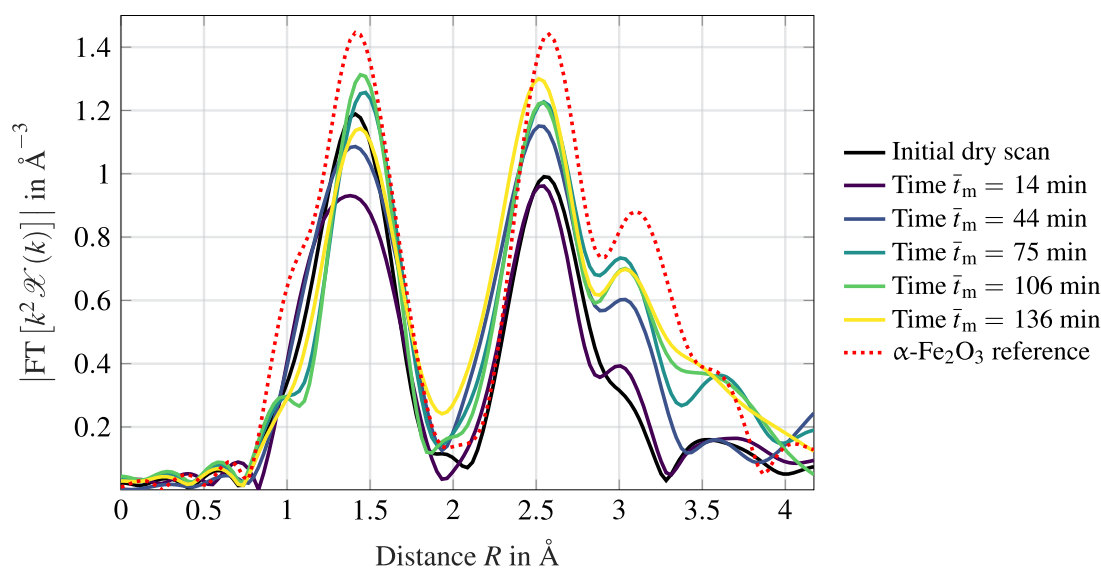


FIG. 14. Fourier transformed (k^2 -weighted) EXAFS data at the Fe K-edge of the α/γ - Fe_2O_3 particles compared to α - Fe_2O_3 during dissolution, all recorded in fluorescence mode (not corrected for phase shift).

dissolution process but rather a result of interaction with reaction products in solution, contingent on the specific experimental boundary conditions explored here.

After evaluating the pure α -phase, in a next step, the dissolution of mixed-phase particles is investigated, which contain besides the α -phase also the γ -phase. During the dissolution of the α/γ - Fe_2O_3 particles, the pre-edge of the XAS spectra changes in intensity and shape, as shown in Fig. 13 (obtained from the merge of the spectra displayed in Figs. 33 and 15 in Appendix B). The pre-edge evolved into a step-like shape, with a notable increase in absorption around 7118 eV, while the characteristic spinel-phase peak near 7114 eV became less prominent. The observed evolution of the Fe K XAS pre-edge is attributed to increasing disorder caused by vacancies in the crystal as the acid attacks the exposed surface of the α/γ - Fe_2O_3 particles^{99–101} (see Sec. III A). Furthermore, the rise in intensity could be due to the bulk sensitivity of XAS: as surface iron is progressively solubilized, the surface-to-volume ratio increases, making the surface disorder more prominent in the spectra over time. As noted by Farges, Brown, and Rehr¹¹⁹ for Ti oxides, increasing disorder broadens both pre-edge and EXAFS features due to averaging over different absorber configurations in the measurement spot.

Examining the EXAFS data, as shown in Fig. 14, reveals changes both in peak positions and in magnitude as the reaction progresses. The shift in signal magnitude is unexpected, as the phase decoherence introduced by the dissolution process should rather lead to a Debye–Waller-like attenuation of $\chi(E)$.¹¹⁹ As depicted in Fig. 13 (for intensity) and Fig. 14 (for magnitude), the rate of these changes slows over time, indicating that the system is stabilizing toward a final state. Comparing the evolution of the spectra with the dry scans (shown in Fig. 24) shows a striking similarity between the final

scans and those of α - Fe_2O_3 , suggesting that the solubilization of the γ -phase proceeds faster than that of the α -phase. As a result, the remaining sample consists increasingly of the α -phase. In addition, the apparent distance in the first coordination shell decreases with time, which may be attributed to the formation of tetrahedral vacancies in the crystal structure. This selective dissolution might also explain the observed pre-edge shape change, where the increasing disorder not only enhances the overall intensity but also contributes to a greater fraction of quadrupolar $1s \rightarrow 3d$ transitions associated with the rhombohedral hematite lattice. The higher reaction rate associated with the spinel structure is well-documented, as outlined in Sec. I, but this behavior has not been previously reported for mixed-phase particles. Neither metallic iron nor humboldtine traces are visible in the EXAFS data (refer to Figs. 16 or 25), even though they are often associated with γ - Fe_2O_3 and reported in studies of other spinel-type oxides such as magnetite³⁷ and given the differing results presented for pure γ - Fe_2O_3 dissolution in Fig. 15. In the case of α/γ - Fe_2O_3 particles, there are no Fe^{II} sites in the crystal that would directly form $\text{Fe}^{\text{II}}\text{C}_2\text{O}_4$. Similar to the α - Fe_2O_3 dissolution, the absence of humboldtine can be explained by the rapid transport of reaction products away from the site, preventing the stable aggregation of Fe–C at the surface to be detected by XAS. The dissolution of pure spinel-type oxides results in the formation of an amorphous structure on the particle surface, as discussed in the following paragraph.

Turning next to the spinel-type pure oxides, the dissolution of magnetite is marked by an increasing intensity of the pre-edge features, alongside a shift in the edge position toward lower energies. This change, indicative of particle reduction, is also observed for maghemite dissolution (Fig. 39 in Appendix B), which contains only Fe^{III} in the crystal. While for magnetite, this effect could be

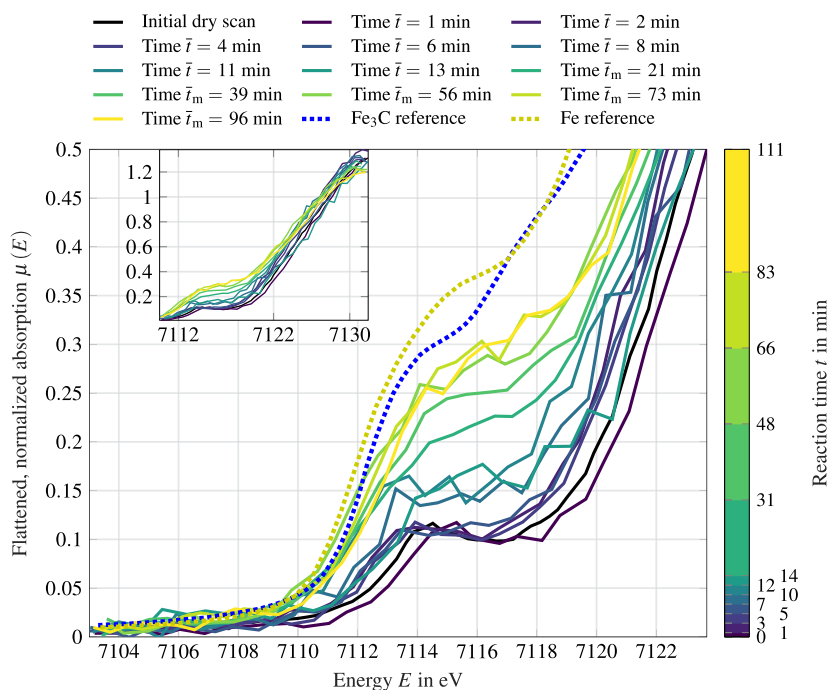


FIG. 15. Evolution of the pre-edge of Fe K XAS for the Fe_3O_4 particles during dissolution without light, recorded in fluorescence mode. The inset displays the evolution of XANES region in detail.

confounded with the significantly smaller particle size (see Sec. III A), the maghemite particles are among the largest of the reference oxides. In addition, the XRD analysis suggests that the crystallite size of the magnetite sample is actually greater than the hematite sample. Thus, it is proposed that this spectral evolution is driven not by the oxidation state, but rather by the crystal structure. For both Fe_3O_4 and $\gamma\text{-Fe}_2\text{O}_3$, $\mu(E)$ initially changes in a non-monotonic manner, eventually becoming strictly monotonic with time, as shown in Fig. 15. Given the continuous reduction, it can be inferred that electron transfer into the crystal lattice plays a more significant role than the solubilization of ferrous iron. If solubilization were dominant, a rise in the bulk oxidation state, indicative of a higher Fe^{III} percentage inside the particles, would be expected. Compared to the pre-edge evolution of $\alpha/\gamma\text{-Fe}_2\text{O}_3$ (Fig. 13), both the rate of change and normalized absorption values are greater for magnetite and maghemite. By observing the spectra during the later stages of the experiment, it becomes clear that $d\mu(E)/dt$ is time-dependent, reaching a maximum at intermediate points, with two minima at the beginning and end. As mentioned in Sec. I, the initial incubation period can be shortened by exposing the sample to UV light (see Figs. 37 and 38 in Appendix B).

When comparing the obtained results to others reported in the literature, the evolution of the pre-edge resembles that observed for progressively higher Fe content during the scanning of a layered iron corrosion sample with a metallic core,⁸⁴ or for the increasing reduction of hematite to metallic iron through Li intercalation.¹²⁰ To highlight these similarities, the reference spectra for Fe and Fe_3C are presented in Fig. 15. Besides these examples, in the context of structured iron oxide particles, a similar shift in the pre-edge can be observed for core-shell nanoparticles with a progressively larger metallic iron core surrounded by a shell of $\gamma\text{-Fe}_2\text{O}_3$ and Fe_3O_4 .¹²¹ Interestingly, both the evolution of the pre-edge toward higher and the white-line toward lower $\mu(E)$ values, shown in

the inset of Fig. 15, contrast with the spectral features of humboldtine (shown in Fig. 25 in Appendix A). This suggests that if the reaction results in the gradual formation of an iron oxalate product under these experimental boundary conditions, it does not conform to the ideal crystalline structure in the early stages of the reaction.

Considering the examples from the literature, although it might be tempting to explain the evolution of the pre-edge as a linear combination of elemental iron, iron carbide, and magnetite or maghemite, no satisfactory combination was found that includes these spectra along with humboldtine and the other reference oxides in Sec. III A. The Linear Combination Analysis (LCA) procedure employed is described in Appendix D, including some example fits (Figs. 54 and 55). A methodological issue contributing to the inadequate LCA results may be the presence of metallic iron. For instance, in the case of layered iron corrosion, it was demonstrated that the presence of metallic iron ($\alpha\text{-Fe}$ or Fe_3C) complicates the application of LCA for accurately identifying the sample composition.⁸⁴ In addition, metallic iron has been shown to interfere with the determination of pre-edge intensity and energy position, making it difficult to resolve the oxidation state accurately. More fundamentally, applying LCA to a complex structure that does not align with reference crystal structures may lead to erroneous conclusions. While we suspect that the presence of carbon in the spectra is due to the interaction of oxalate ions with the surface,¹¹⁷ it is unlikely that the structure corresponds to common iron carbides or other forms listed in the literature.¹²²

For a deeper understanding of the structural changes over time, the EXAFS data shown in Fig. 16 were obtained according to the procedure described in Sec. II D. As the reaction progresses, the EXAFS features generally broaden and attenuate, which can be attributed to absorber averaging and phase decoherence effects, respectively,¹¹⁹ as described for the $\alpha/\gamma\text{-Fe}_2\text{O}_3$ particles. Notably,

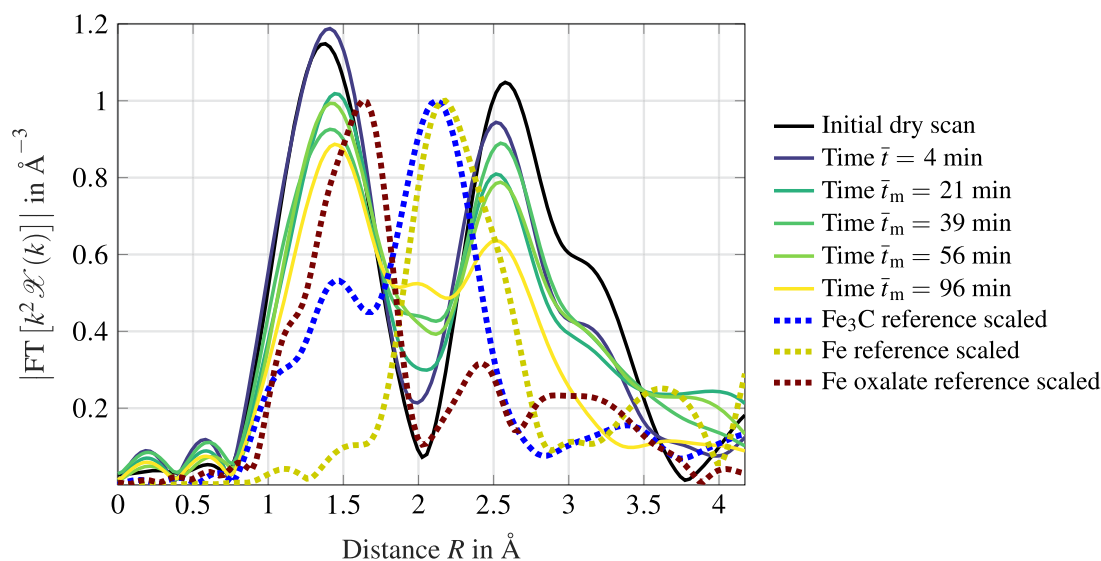


FIG. 16. Fourier transformed (k^2 -weighted) EXAFS data at the Fe K-edge of the Fe_3O_4 particles during dissolution compared to selected references, all recorded in fluorescence mode (not corrected for phase shift).

the distance of the first coordination shell increases, while the distance of the second coordination shell decreases over time. This behavior, observed for the α/γ -Fe₂O₃ particles as well, may be due to the formation of vacancies as the primary crystal dissolves. A distinctive feature is the increasing prominence of a peak at ~ 2 Å in the later stages of the experiment. This position is close to, but not identical with, the peak position of Fe₃C or Fe. For clarity, the EXAFS of the references in Fig. 16 have been normalized to their individual maxima, since their $\mathcal{X}(k)$ oscillations result in FT magnitudes exceeding 3 \AA^{-3} . Similar to the pre-edge analysis, the choice between Fe and Fe₃C remains ambiguous due to the lack of distinguishing features, and the long-range interactions assume an ideal crystal configuration.

In the literature, for core-shell iron oxide nanoparticles, an increasing Fe content in the core has been associated with a similar rise in the peak between the two coordination shells, which has been linked to α -Fe.¹²¹ In the context of electrochemistry, the EXAFS features observed in Fig. 16 exhibit striking similarities to the EXAFS evolution observed during the first discharge in a charging/discharging cycle of a magnetite electrode in a Li ion battery.¹²³ Although the mechanisms involved differ from those in the dissolution experiments of the current study, this example provides additional insights into how EXAFS data can change with varying crystal structures. During the charge process, there is an initial intercalation of Li atoms into the magnetite crystal, followed by a gradual reduction to FeO, and eventually a sudden increase in metallic iron concentration. In this case, the increasing peak prominence at 2 Å was attributed to the increasing metallic iron content, while the decrease in intensity at 3 Å was related to the decrease in tetrahedral Fe coordination with increasing Li insertion. However, in the dissolution experiments of this study, if the decrease in intensity is indeed related to a reduction in tetrahedral Fe coordination, the underlying cause remains ambiguous. It could be influenced either by the preferential solubilization of tetrahedrally coordinated Fe or by the increasing concentration of a product lacking tetrahedral components in its structure.

In summary, it becomes evident that the crystal structure, rather than the oxidation state, is the primary factor influencing the reaction mechanisms. The non-reductive mechanism is associated with the pure α -phase, whereas the reductive mechanism is more relevant for the pure γ -phase. When comparing the evolution of the obtained spectra with other reduction processes in the literature and pure oxide spectra, it appears that the reductive mechanism leads to the gradual formation of an amorphous structure rather than the direct formation of crystalline humboldtine. Interestingly, despite the considerable content of the γ -phase in the mixed-phase particles, no reduction was observed. Instead of a straightforward reductive dissolution proportional to the γ -phase content, a preferential detachment of the tetrahedrally coordinated iron atoms was noted. This gradual transition to a pure α -phase illustrates that the effect of a mixed phase on particle properties extends beyond a simple linear combination of the two mechanisms, resulting in distinct reaction.

Finally, considering that light, particularly in the UV spectrum, influences the reaction mechanisms,^{19–21} the impact of light exposure was tested for both Fe₃O₄ and α/γ -Fe₂O₃ particles (see Sec. II B). The Fe₃O₄ oxide was chosen due to its expected strong

effect from the spinel structure and Fe^{II} in the crystal, while α/γ -Fe₂O₃ was selected based on its previous use in a batch reactor study.¹⁹ For Fe₃O₄, the addition of UV light accelerated the reaction in the initial stages, but both the pre-edge and EXAFS analyses converged to the same final values as those observed without light. No significant effect of UV light on the pre-edge or EXAFS was observed for the α/γ -Fe₂O₃ particles (refer to Sec. III B 1). Given that the spectral features of other oxides are expected to be less pronounced than those of Fe₃O₄ or α/γ -Fe₂O₃, the UV lamp was turned off for all other experiments.

2. Dissolution of combusted iron particles

Figure 17 shows the pre-edge evolution during the dissolution of CIPs, $\Phi = 1.5$. With increasing reaction time, the spinel-associated peak at ~ 7114 eV becomes less prominent, comparable to the spectra obtained for the α/γ -Fe₂O₃ particles. However, this effect is absent in the other CIP experiments and could be confounded by the general increase in intensity due to more dissolution-induced vacancies, as discussed in Sec. III B 1. As depicted in the inset of Fig. 17, the energy of the edge position decreases with time. However, the change is only minor at less than 1 eV, which is within the range of experimental uncertainty.⁶⁹ As discussed in Sec. III A, the CIPs contain both the α - and γ -phases, similar to the α/γ -Fe₂O₃ particles. Considering the spectral evolution for the α/γ -Fe₂O₃ particles, it is therefore unexpected that the dissolution of the CIPs proceeds with almost no discernible change in the spectra. This is despite the significant decrease in the fluorescence signal (see Fig. 31), indicating the solubilization of the iron.

If the particles exhibit indeed a core-shell structure, a gradual transition of the spectra is expected as the hematite shell is gradually dissolved and the magnetite core becomes exposed. There could be an influence of the particle size-selective probing depth of XAS on the obtained spectra (discussed in Sec. III A) due to the core-shell structure, which results in a more hematite-dominated spectrum. However, this effect should become less severe as the reaction progresses. Therefore, it is assumed that the obtained pre-edge evolution is instead caused by the structure of the core. When burning iron particles without propane-assistance, the core particle structure within the hematite shell shown by Choizez *et al.*⁶⁵ is not actually entirely magnetite, rather it has hematite interstitials. The almost constant normalized spectra of the CIPs may thus be caused by the hematite shell and interstitials that block the access of OxA to the magnetite core. This structural difference could also explain the disparity between the α/γ -Fe₂O₃ and CIPs polymorphs, despite their bulk similarity in containing both α - and γ -phases. The more pronounced evolution of the pre-edge for the particular experimental run in Fig. 17 could be not only due to the higher magnetite content at $\Phi = 1.5$ compared to the other CIP experiments but also due to the sampling from a highly polydisperse system. A replicate of the $\Phi = 1.5$ and $\Phi = 0.67$ CIP dissolution experiments is shown in Figs. 40 and 41, respectively, in Appendix B. In contrast to the CIPs fixed in the granular bed, the iron-bearing compounds in the accumulated liquid product after conclusion of the experiment resemble very closely the spectrum of humboldtine (displayed in Figs. 52 and 53).

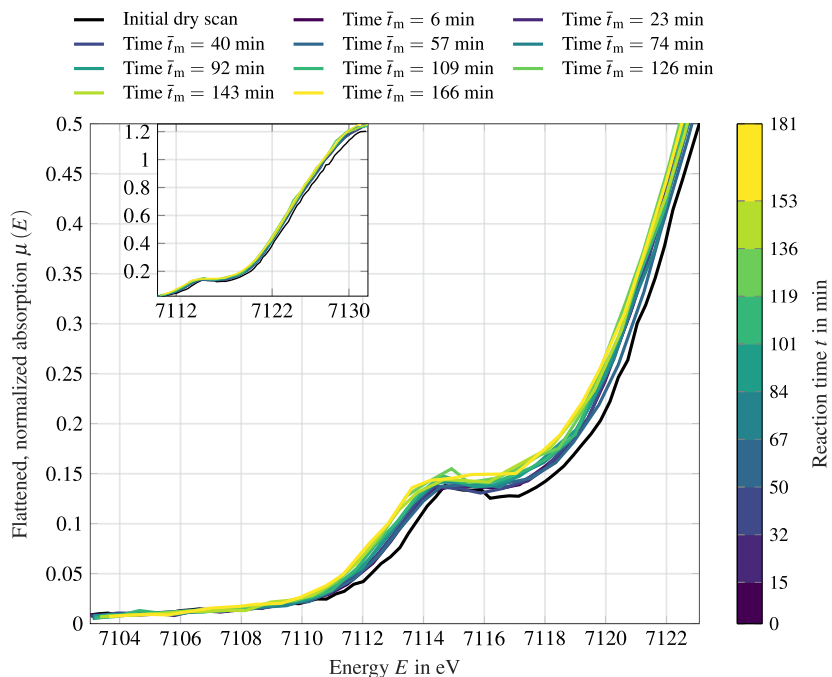


FIG. 17. Evolution of the pre-edge of Fe K XAS of the $\Phi = 1.5$ particles during dissolution without light, fluorescence mode. The inset displays the XANES evolution in detail.

IV. SUMMARY AND CONCLUSION

In this study, *in situ* XAS was employed to gain insights into the dissolution mechanisms of both pure iron oxides and mixed phase particles in aqueous OxA (0.5 mol/l). Prior to dissolution, the morphology, composition, and oxidation state of the particles were determined using a combination of complementary techniques (SEM, μ CT, Mössbauer spectroscopy, XRD, XANES, and EXAFS). The CIPs were found to consist mainly of a partially hollow structure of α -Fe₂O₃ and Fe₃O₄, with an increasing Fe₃O₄ content as the combustion fuel-to-air equivalence ratio, Φ , increases. Dissolution experiments were performed in a temperature-controlled, continuous-flow capillary reactor, allowing the removal of reaction products, thereby suppressing the autocatalytic reaction mechanism. The non-reductive dissolution of α -Fe₂O₃ was confirmed by *in situ* XAS, while spinel-type oxides such as γ -Fe₂O₃ and Fe₃O₄ showed reductive dissolution, indicated by shifts in edge position and changes in the pre-edge of XANES spectra and EXAFS features. The formation of a complex amorphous structure, which is not identical to α -Fe or Fe₃C, is proposed. For particles with mixed α - and γ -phases (α/γ -Fe₂O₃), the preferential non-reductive dissolution of the γ -phase was observed, which demonstrates that the effect of a mixed phase extends beyond a simple linear combination of the single phases. Despite similar bulk phase mixtures, CIPs predominantly underwent non-reductive dissolution without any change in their structure, highlighting the importance of the internal Fe phase structure in controlling the dissolution process. Humboldtine-like species (Fe^{II}C₂O₄·2H₂O) detected in the solution but not on the particle surface indicates that it is not formed as an inherent dissolution step during surface reactions. Furthermore, variations in Φ resulted in no changes to the dissolution mechanisms under otherwise identical conditions. This suggests

that a lower Φ , which enhances metal conversion efficiency during combustion, would be more advantageous for iron-based fuel systems. In conclusion, this study demonstrated that the Fe phase composition and structure of the particles are the primary factors determining the reaction mechanisms under the specified conditions, rather than their formal oxidation state.

ACKNOWLEDGMENTS

This work was funded by the Hessian Ministry of Higher Education, Research, Science and the Arts—cluster project Clean Circles as well as the Karlsruhe Institute of Technology (KIT). We acknowledge the Institute for Beam Physics and Technology (IBPT) for the operation of the storage ring, the Karlsruhe Research Accelerator (KARA). We thank L. Braun and B. Stumpf for their help during the preparation and performing of the experiments. We also thank M. Fedoryk and D. Trimis for providing the combusted iron particles, the Institute of Materials Science at the Technical University Darmstadt for the access to the scanning electron microscope, and J. Schmidpeter and P. Neuhäusel in particular for their help during its operation. The x-ray computed tomography experiments were performed at the Institute for Applied Materials (IAM) at the Karlsruhe Institute of Technology (KIT). Parts of this work have been improved grammatically and stylistically using language models, including ChatGPT (OpenAI) and DeepL Write (DeepL SE).

AUTHOR DECLARATIONS

Conflict of Interest

The authors have no conflicts to disclose.

Author Contributions

M. Lausch: Formal analysis (equal); Investigation (equal); Methodology (equal); Software (equal); Validation (equal); Visualization (equal); Writing – original draft (equal). **A. Zimina:** Formal analysis (equal); Investigation (equal); Supervision (equal); Writing – original draft (equal); Writing – review & editing (equal). **J. Bao:** Formal analysis (supporting); Investigation (equal); Writing – original draft (supporting). **R. Pashminehazar:** Investigation (equal). **B. J. M. Etzold:** Conceptualization (equal); Funding acquisition (equal); Resources (equal); Supervision (equal); Writing – review & editing (equal). **U. I. Kramm:** Conceptualization (equal); Funding acquisition (equal); Supervision (equal); Writing – review & editing (equal). **J.-D. Grunwaldt:** Conceptualization (equal); Funding acquisition (equal); Supervision (equal); Writing – review & editing (equal). **J. Hussong:** Conceptualization (equal); Funding acquisition (equal); Supervision (equal); Writing – review & editing (equal).

DATA AVAILABILITY

The data that support the findings of this study are available from the corresponding author upon reasonable request.

APPENDIX A: PARTICLE CHARACTERIZATION

Figures 18–28 show the simulated XRD peaks for selected iron oxides; reference iron oxides compared against their

theoretical diffraction patterns; pre-edge fit of γ -Fe₂O₃ absorption data; pre-edge fit of Fe absorption data; the Extended X-ray Absorption Fine Structure (EXAFS) for selected iron oxides; k^2 -weighted $\chi(k)$ for selected iron oxides; Fourier transformed (k^2 -weighted) EXAFS data at the Fe K-edge, normalized by their individual maximum; Fourier transformed (k^2 -weighted) EXAFS data at the Fe K-edge for selected iron-bearing references; k^2 -weighted $\chi(k)$ for selected iron-bearing references; lower magnification scanning electron microscopy image of combusted iron particles; and particle size distribution for selected reference oxides determined by laser diffraction particle size analysis, respectively.

APPENDIX B: DISSOLUTION EXPERIMENTS

Figures 29–31 show the fluorescence x-ray absorption spectroscopic data at the Fe K-edge of the α -Fe₂O₃ particles, fluorescence x-ray absorption spectroscopic data at the Fe K-edge of the Fe₃O₄ particles, and fluorescence x-ray absorption spectroscopic data at the Fe K-edge of the combusted iron particles, $\Phi = 1.5$, respectively.

1. Pre-edge features

a. Hematite and mixed iron(III) oxide particles

Figures 32–35 show the evolution of the pre-edge of Fe K XAS of the α -Fe₂O₃ particles (second repetition), evolution of the pre-edge of Fe K XAS of the α/γ -Fe₂O₃ particles (first rep-

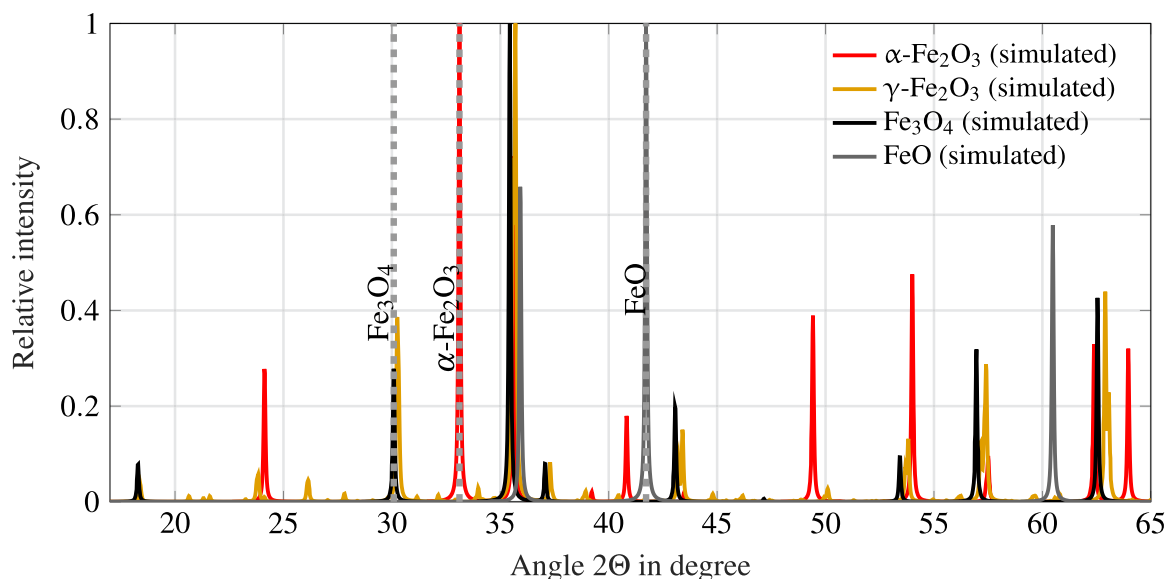


FIG. 18. Simulated XRD peaks for selected iron oxides, scaled by their individual maximum.

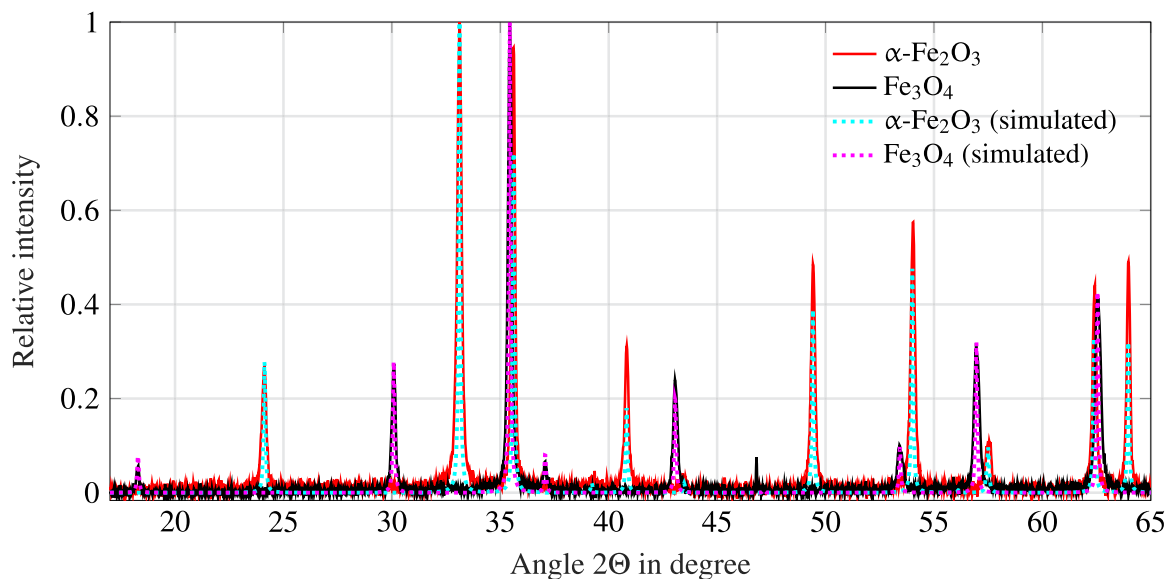


FIG. 19. Reference iron oxides and their theoretical diffraction patterns, scaled by their individual maximum.

etition), evolution of the pre-edge of Fe K XAS of the α/γ - Fe_2O_3 particles (second repetition), and evolution of the pre-edge of Fe K XAS of the α/γ - Fe_2O_3 particles during dissolution, respectively.

2. Dissolution of magnetite and maghemite particles

Figures 36–39 show the evolution of the pre-edge of Fe K XAS of the Fe_3O_4 particles without light (second repetition), evolution of the pre-edge of Fe K XAS of the Fe_3O_4 particles with light (first repetition), evolution of the pre-edge of Fe K XAS of the Fe_3O_4 particles with light (second repetition), and evolution of the pre-edge of Fe K XAS of the γ - Fe_2O_3 particles during dissolution without light, respectively.

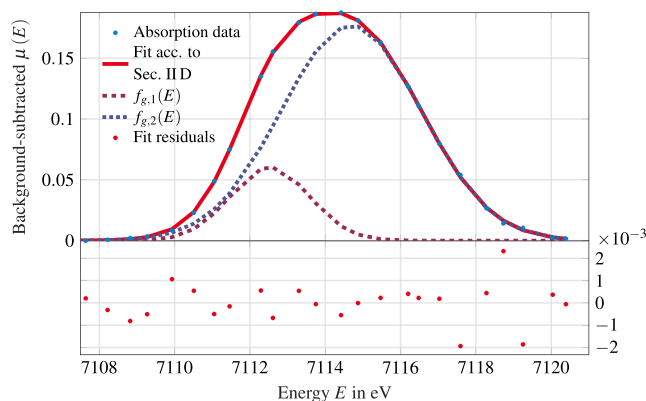


FIG. 21. Pre-edge fit of Fe absorption data.

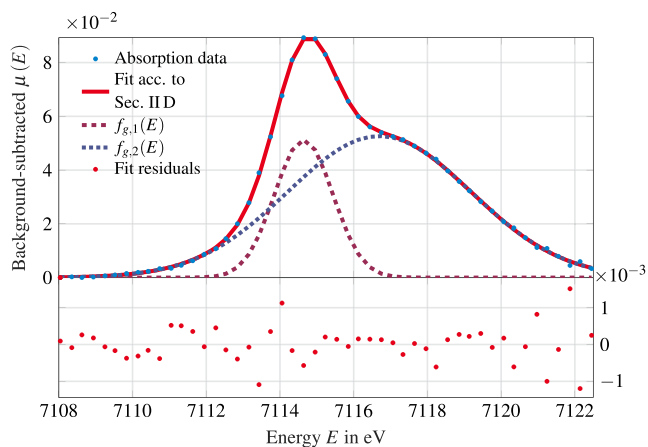


FIG. 20. Pre-edge fit of γ - Fe_2O_3 absorption data.

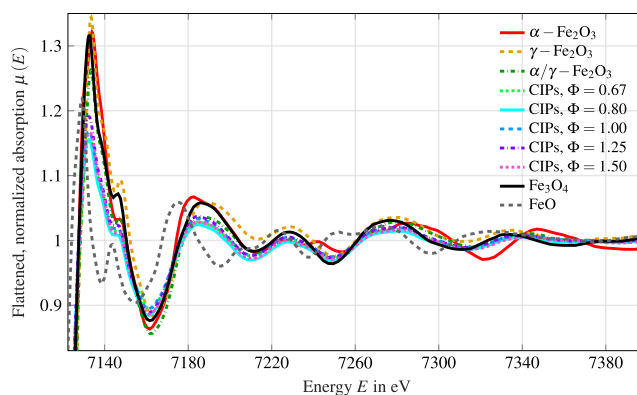


FIG. 22. Extended X-ray Absorption Fine Structure (EXAFS) detail in the recorded spectra.

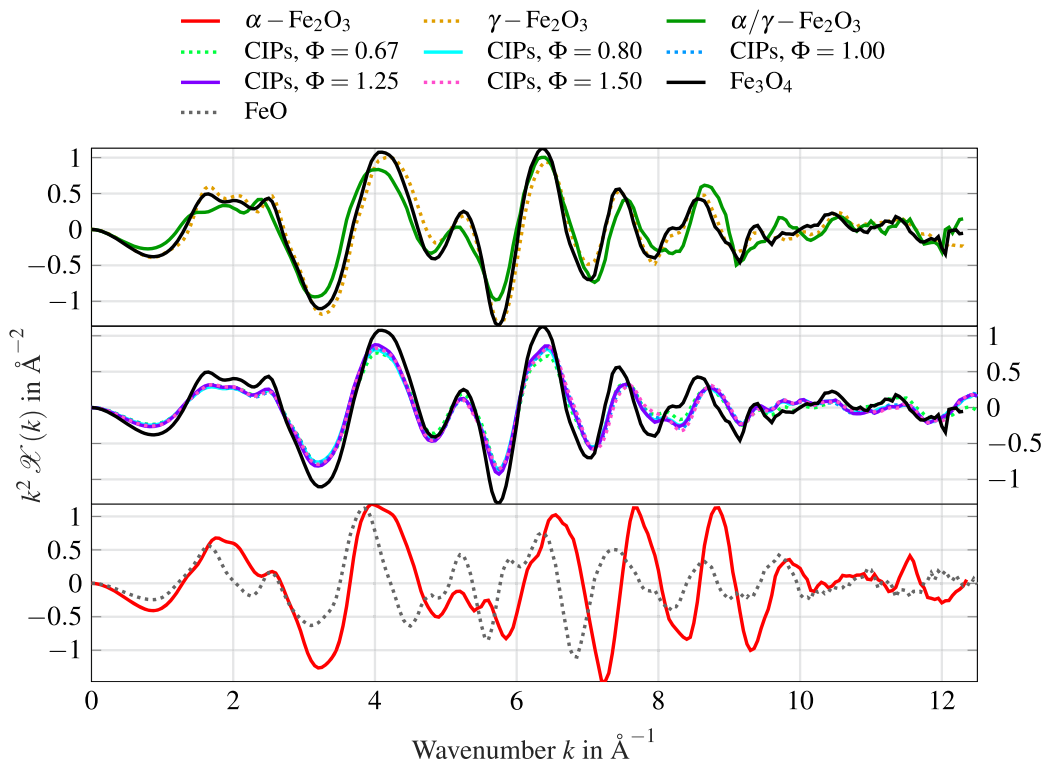


FIG. 23. k^2 -weighted $\chi(k)$ for selected iron oxides.

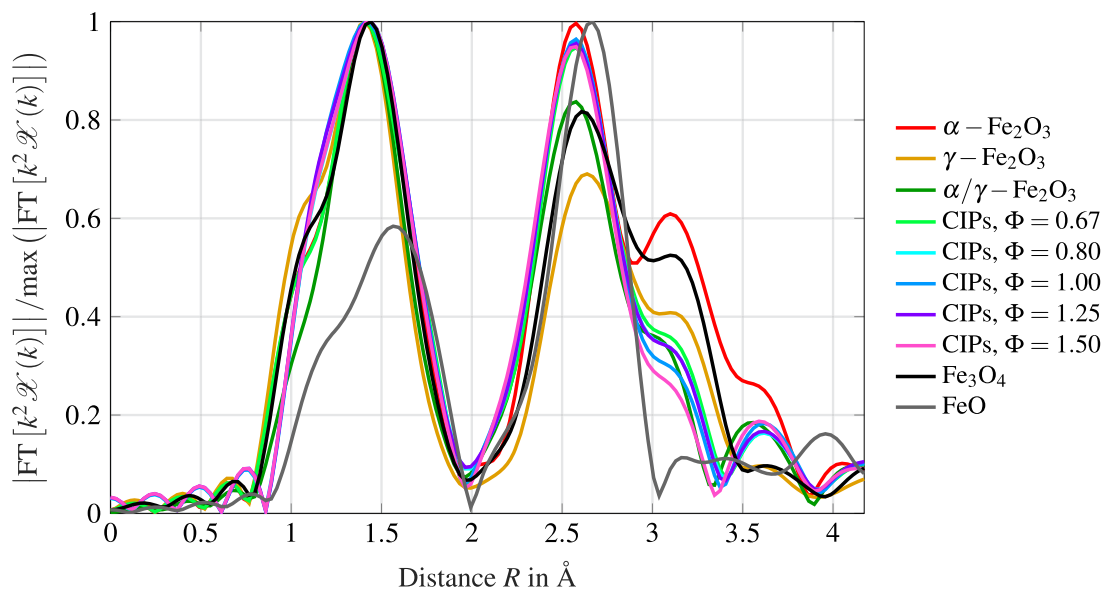


FIG. 24. Fourier transformed (k^2 -weighted) EXAFS data at the Fe K-edge, normalized by their individual maximum, of the combusted iron particles (CIPs) for varying fuel-to-air equivalence ratio Φ in comparison with reference oxides, all recorded in transmission mode (not corrected for phase shift).

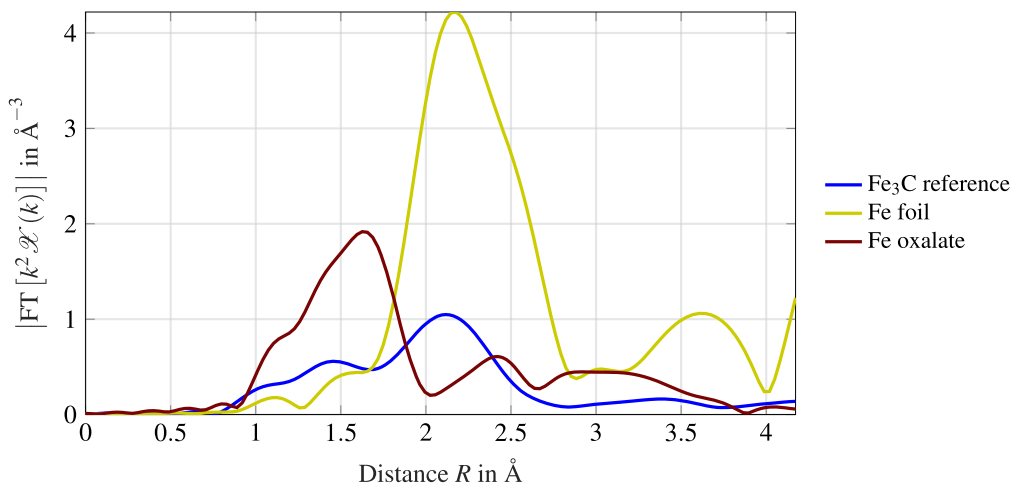


FIG. 25. Fourier transformed (k^2 -weighted) EXAFS data at the Fe K-edge for selected iron-bearing references, all recorded in transmission mode (not corrected for phase shift).

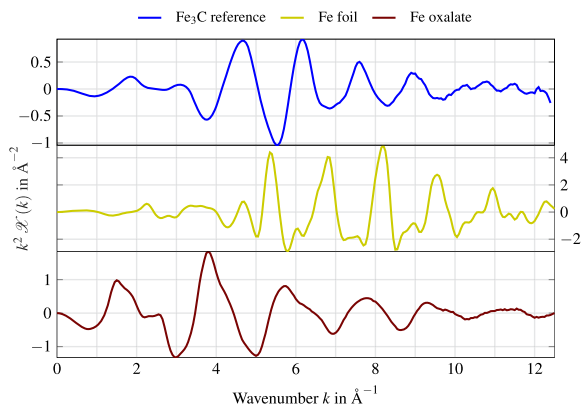


FIG. 26. k^2 -weighted $\chi(k)$ for selected iron-bearing references.

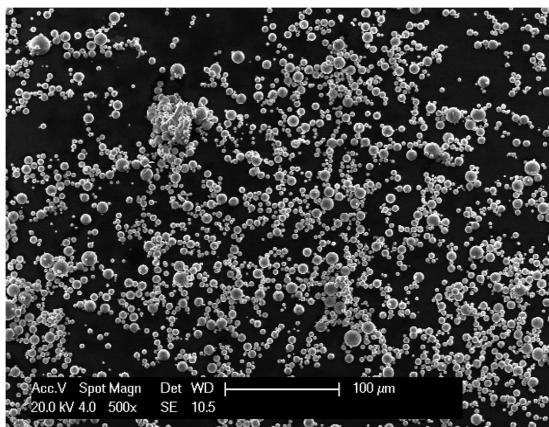


FIG. 27. Lower magnification Scanning Electron Microscopy (SEM) particle image of Fig. 9(f).

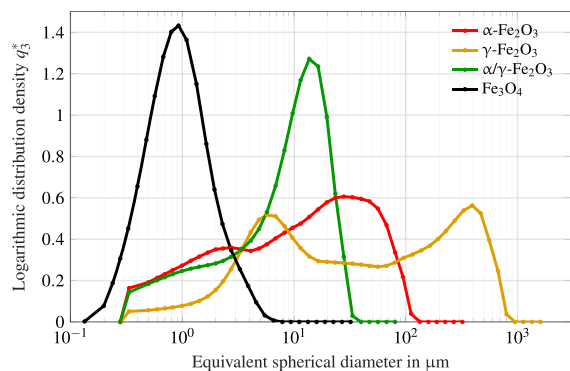


FIG. 28. Particle size distribution for selected reference oxides determined by laser diffraction particle size analysis (Sympatec GmbH, dry dispersion using the RODOS system and measurement using the HELOS system).

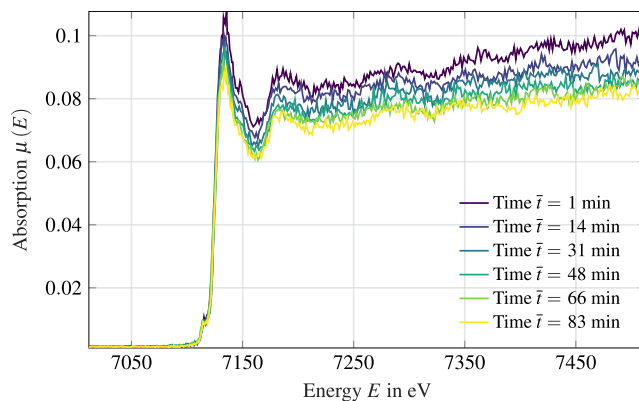


FIG. 29. Fluorescence x-ray absorption spectroscopic data at the Fe K-edge of the α - Fe_2O_3 particles during dissolution with no light.

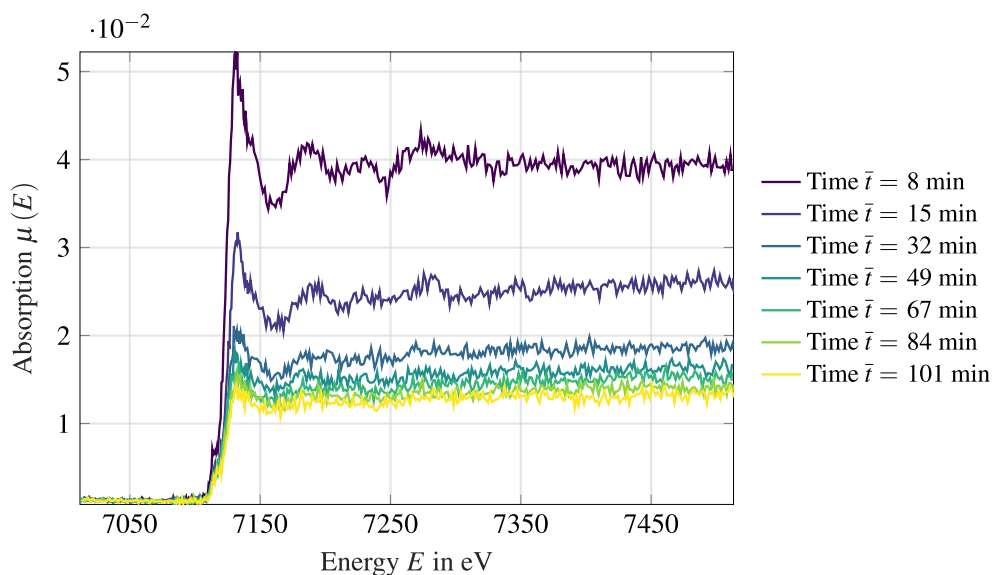


FIG. 30. Fluorescence x-ray absorption spectroscopic data at the Fe K-edge of the Fe_3O_4 particles during dissolution with no light.

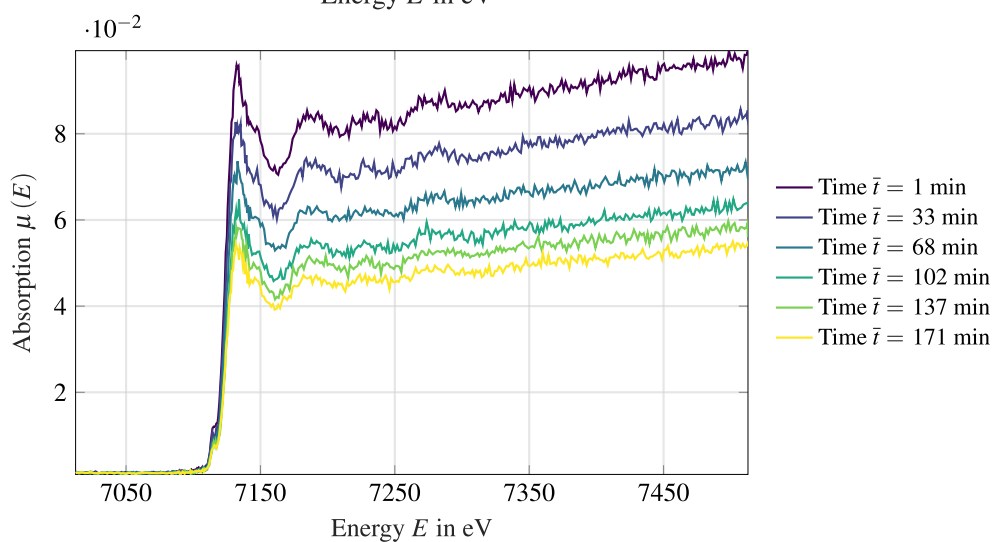


FIG. 31. Fluorescence x-ray absorption spectroscopic data at the Fe K-edge of the $\Phi = 1.5$ particles during dissolution with no light.

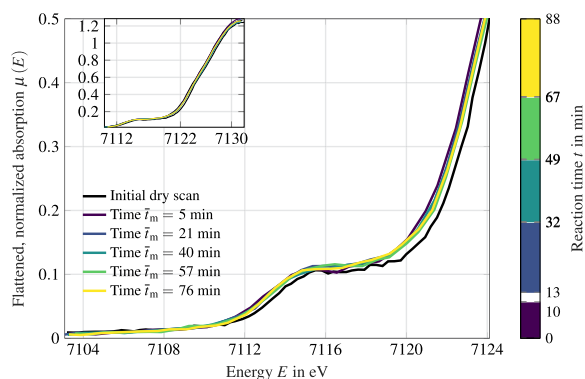


FIG. 32. Evolution of the pre-edge of Fe K XAS of the $\alpha\text{-Fe}_2\text{O}_3$ particles (second repetition) during dissolution without light, all recorded in fluorescence mode. The inset displays the XANES evolution in detail.

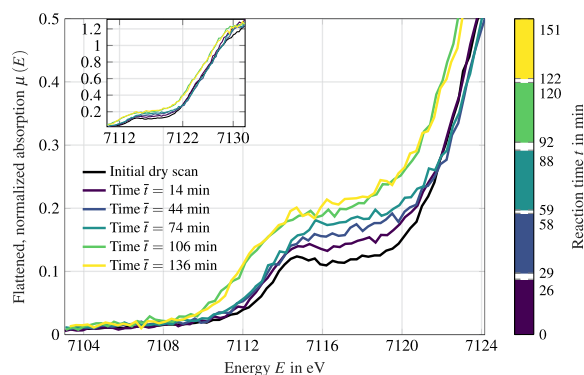


FIG. 33. Evolution of the pre-edge of Fe K XAS of the $\alpha/\gamma\text{-Fe}_2\text{O}_3$ particles (first repetition) during dissolution without light, all recorded in fluorescence mode. The inset displays the XANES evolution in detail.

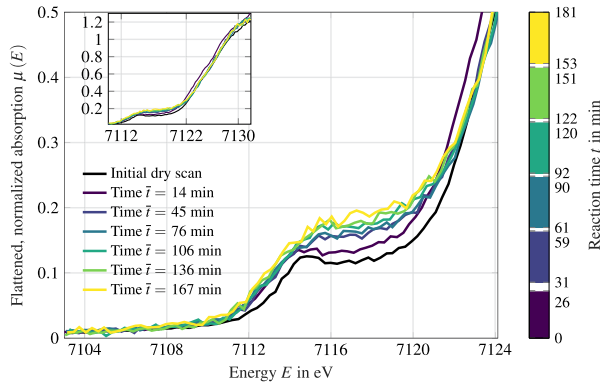


FIG. 34. Evolution of the pre-edge of Fe K XAS of the α/γ - Fe_2O_3 particles (second repetition) during dissolution without light, all recorded in fluorescence mode. The inset displays the XANES evolution in detail.

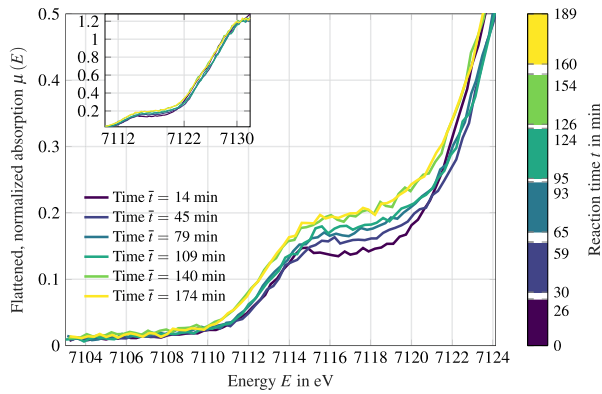


FIG. 35. Evolution of the pre-edge of Fe K XAS of the α/γ - Fe_2O_3 particles during dissolution with light, all recorded in fluorescence mode. The inset displays the XANES evolution in detail.

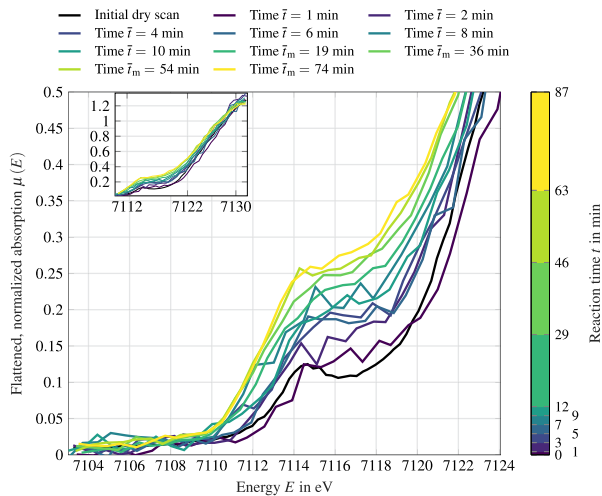


FIG. 36. Evolution of the pre-edge of Fe K XAS of the Fe_3O_4 particles (second repetition) during dissolution without light, all recorded in fluorescence mode. The inset displays the XANES evolution in detail.

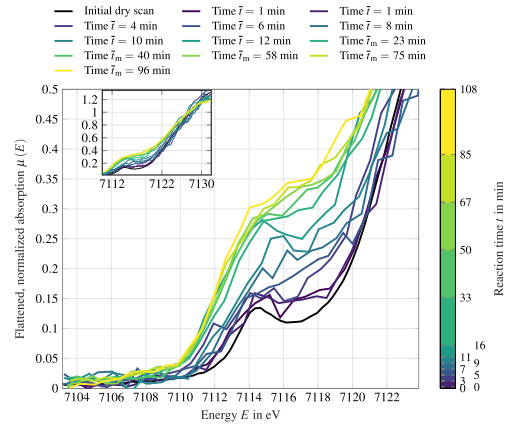


FIG. 37. Evolution of the pre-edge of Fe K XAS of the Fe_3O_4 particles (first repetition) during dissolution with light, all recorded in fluorescence mode. The inset displays the XANES evolution in detail.

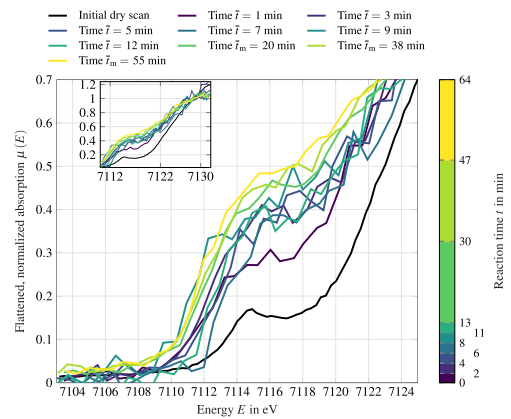


FIG. 38. Evolution of the pre-edge of Fe K XAS of the Fe_3O_4 particles (second repetition) during dissolution with light, all recorded in fluorescence mode. The inset displays the XANES evolution in detail.

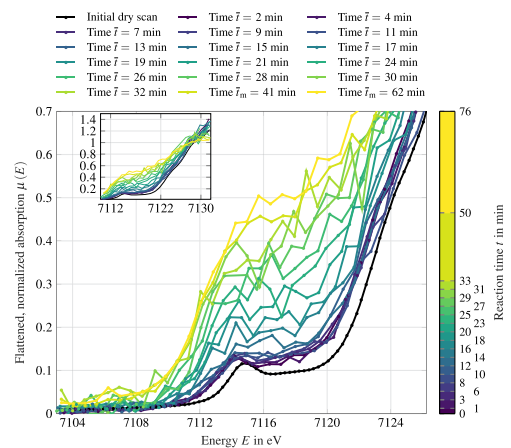


FIG. 39. Evolution of the pre-edge of Fe K XAS of the γ - Fe_2O_3 particles during dissolution without light, all recorded in fluorescence mode. The inset displays the XANES evolution in detail.

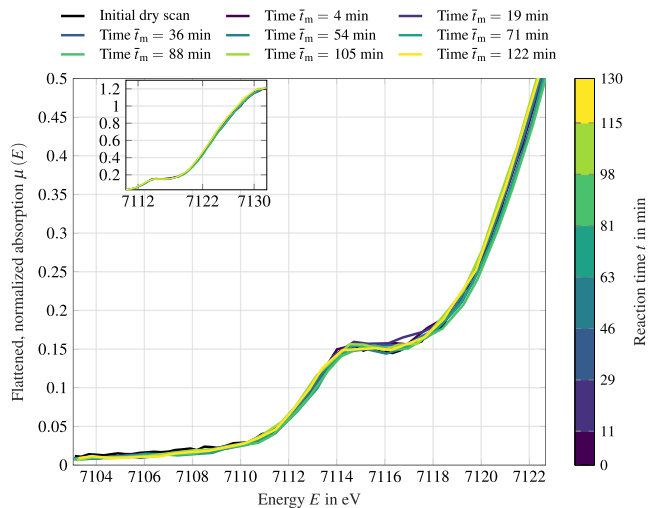


FIG. 40. Evolution of the pre-edge of Fe K XAS of the combusted iron particles, $\Phi = 1.5$ (second repetition), during dissolution without light, all recorded in fluorescence mode. The inset displays the XANES evolution in detail.

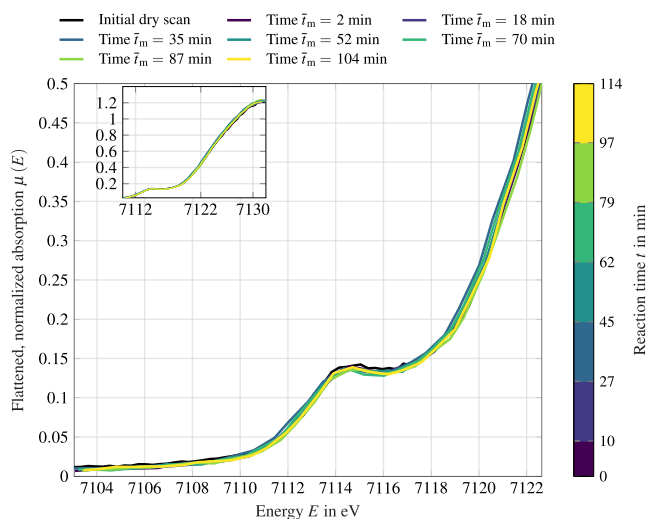


FIG. 41. Evolution of the pre-edge of Fe K XAS of the combusted iron particles, $\Phi = 0.67$, during dissolution without light, all recorded in fluorescence mode. The inset displays the XANES evolution in detail.

3. Dissolution of combusted iron particles

Figures 40 and 41 show the evolution of the pre-edge of Fe K XAS of the combusted iron particles, $\Phi = 1.5$ (second repetition), during dissolution and evolution of the pre-edge of Fe K XAS of the $\Phi = 0.67$ particles during dissolution, respectively.

APPENDIX C: DISSOLUTION EXPERIMENTS—EXAFS DATA

Figures 42–51 show the Fourier transformed (k^2 -weighted) EXAFS data at the Fe K-edge of the Fe_3O_4 particles during dissolution with light, the corresponding k^2 -weighted $\chi(k)$ in Fig. 43, Fourier transformed (k^2 -weighted) EXAFS data at the Fe K-edge of the Fe_3O_4 particles during dissolution without light, the corresponding k^2 -weighted $\chi(k)$ in Fig. 45, Fourier transformed (k^2 -weighted) EXAFS data at the Fe K-edge of the Fe_3O_4 particles during dissolution with light, the corresponding k^2 -weighted $\chi(k)$ in Fig. 47, Fourier transformed (k^2 -weighted) EXAFS data at the Fe K-edge of the $\gamma\text{-Fe}_2\text{O}_3$ particles during dissolution without light, the corresponding k^2 -weighted $\chi(k)$ in Fig. 48, the k^2 -weighted $\chi(k)$ of Fig. 14, associated with the dissolution of $\alpha/\gamma\text{-Fe}_2\text{O}_3$ particles without light, and the k^2 -weighted $\chi(k)$ of Fig. 16, associated with the dissolution of Fe_3O_4 particles without light, respectively.

APPENDIX D: DISSOLUTION EXPERIMENTS—LIQUID PRODUCT

Figures 52 and 53 show the XANES spectra of the liquid product and selected references after reaction with combusted iron particles, $\Phi = 1.5$, and Fourier transformed (k^2 -weighted) EXAFS data at the Fe K-edge of the liquid product and selected references after reaction with combusted iron particles, $\Phi = 1.5$.

1. Linear combination analysis

To attribute the gradual evolution in some of the spectra over time to the build-up of the reaction products, linear combination analysis (LCA) was performed. The LCA was carried out by using the initial dry energy scan of the sample in the capillary and the pellet scans of the other components as references. The energy range of the LCA was selected between 7090 eV and the first isosbestic point at 7152 eV. The references selected included besides the initial dry sample scans all combinations of Fe, FeO, Fe_3C , and Fe oxalates. The best results were obtained for the combination of Fe_3C and the initial dry sample scan. However, even for the best obtained fitting results, there is either a systematic underprediction of the pre-edge intensity or the maximum absorption. Extending the fit range (up to 7250 eV) does not lead to improved fit results. Example fits are presented in Figs. 54 and 55.

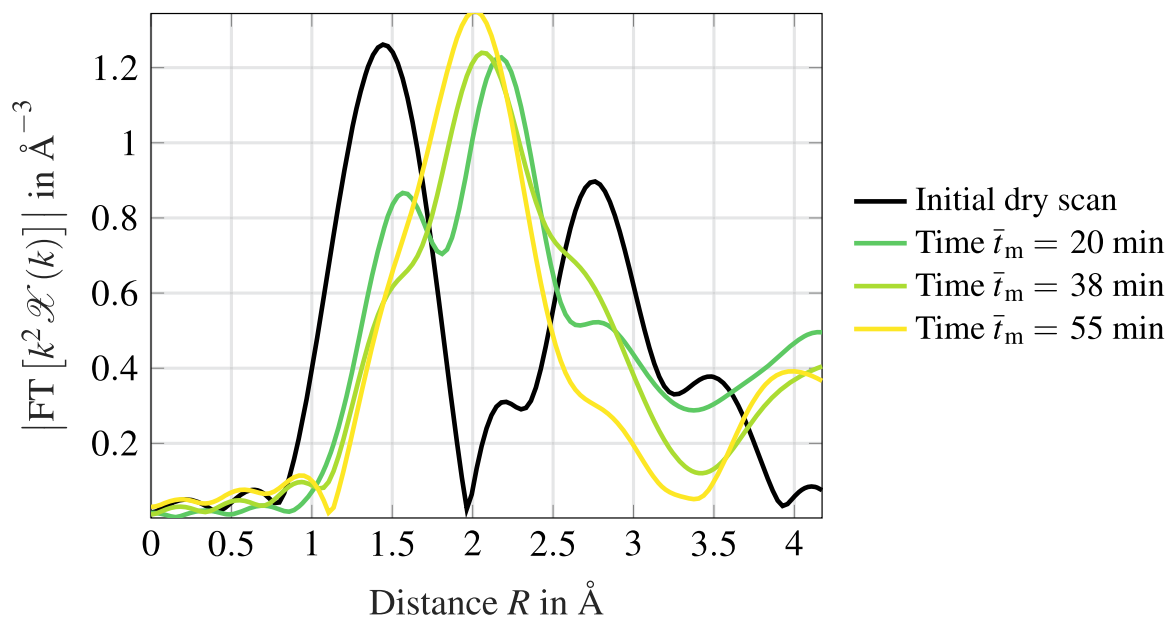


FIG. 42. Fourier transformed (k^2 -weighted) EXAFS data at the Fe K-edge of the Fe_3O_4 particles during dissolution with light, all recorded in fluorescence mode (not corrected for phase shift).

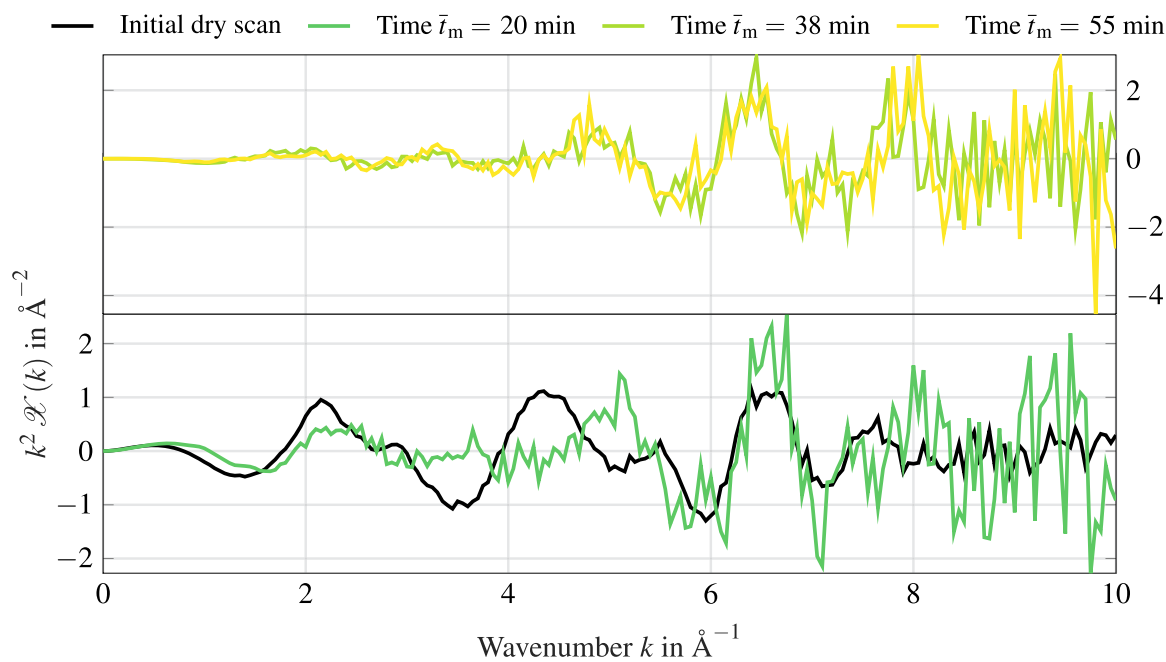


FIG. 43. k^2 -weighted $\chi(k)$ of Fig. 42.

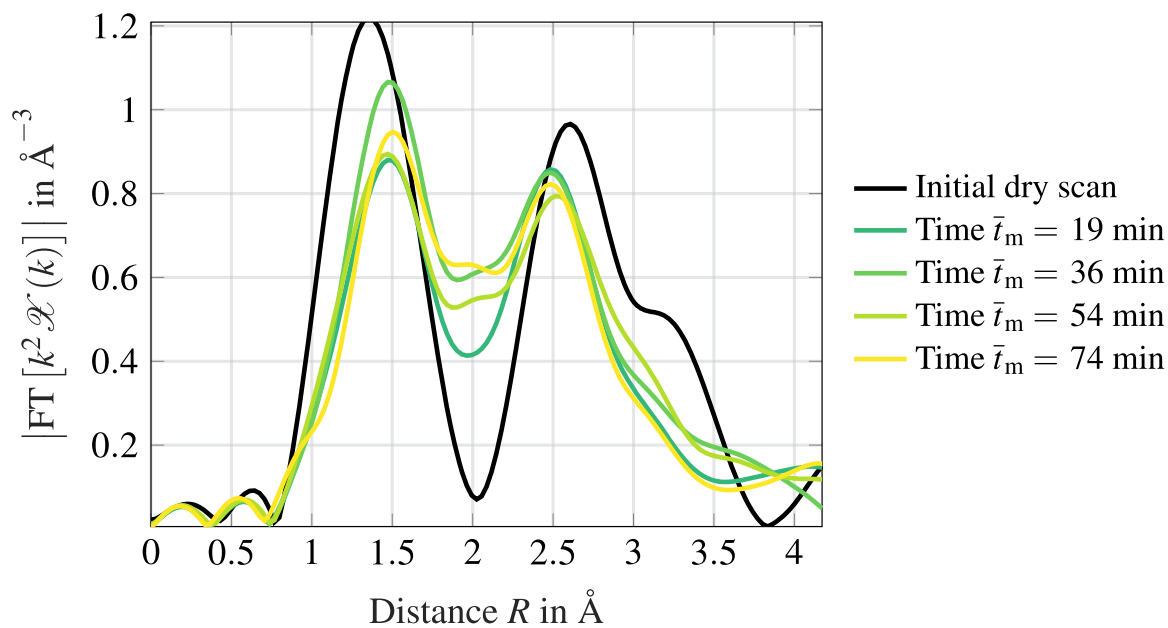


FIG. 44. Fourier transformed (k^2 -weighted) EXAFS data at the Fe K-edge of the Fe_3O_4 particles during dissolution without light, all recorded in fluorescence mode (not corrected for phase shift).

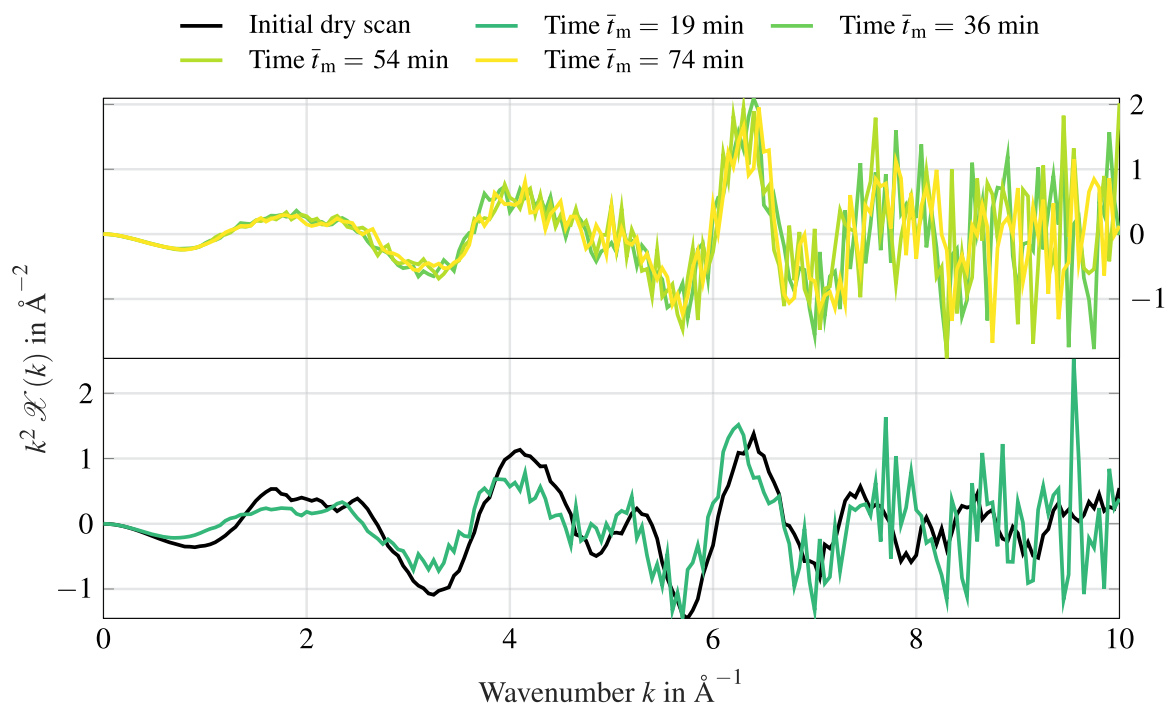


FIG. 45. k^2 -weighted $\chi(k)$ of Fig. 44.

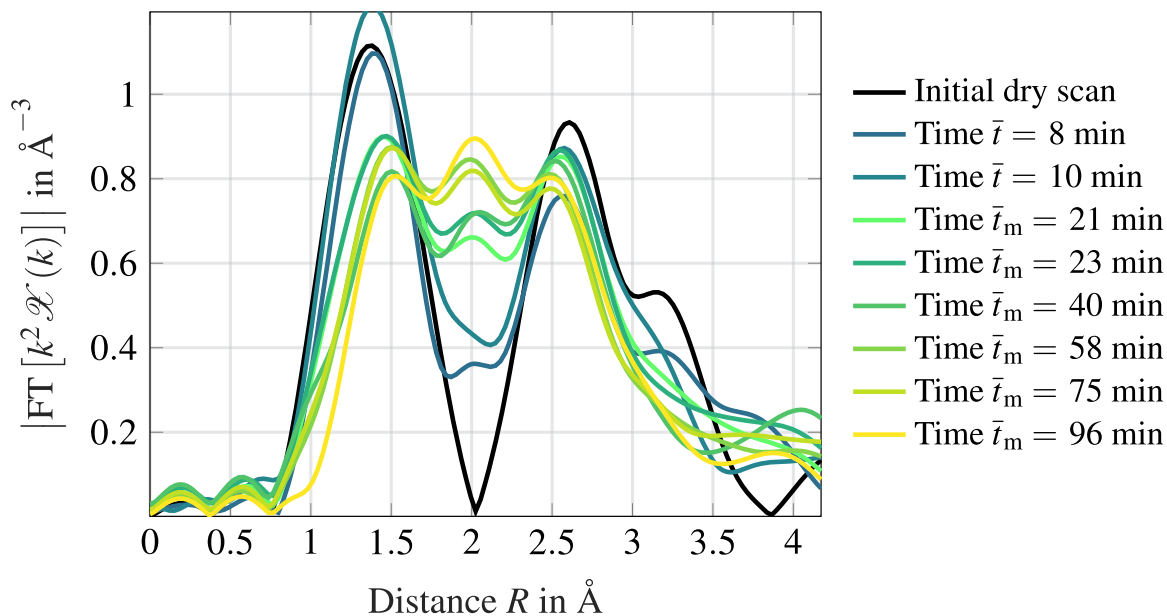


FIG. 46. Fourier transformed (k^2 -weighted) EXAFS data at the Fe K-edge of the Fe_3O_4 particles during dissolution with light, all recorded in fluorescence mode (not corrected for phase shift).

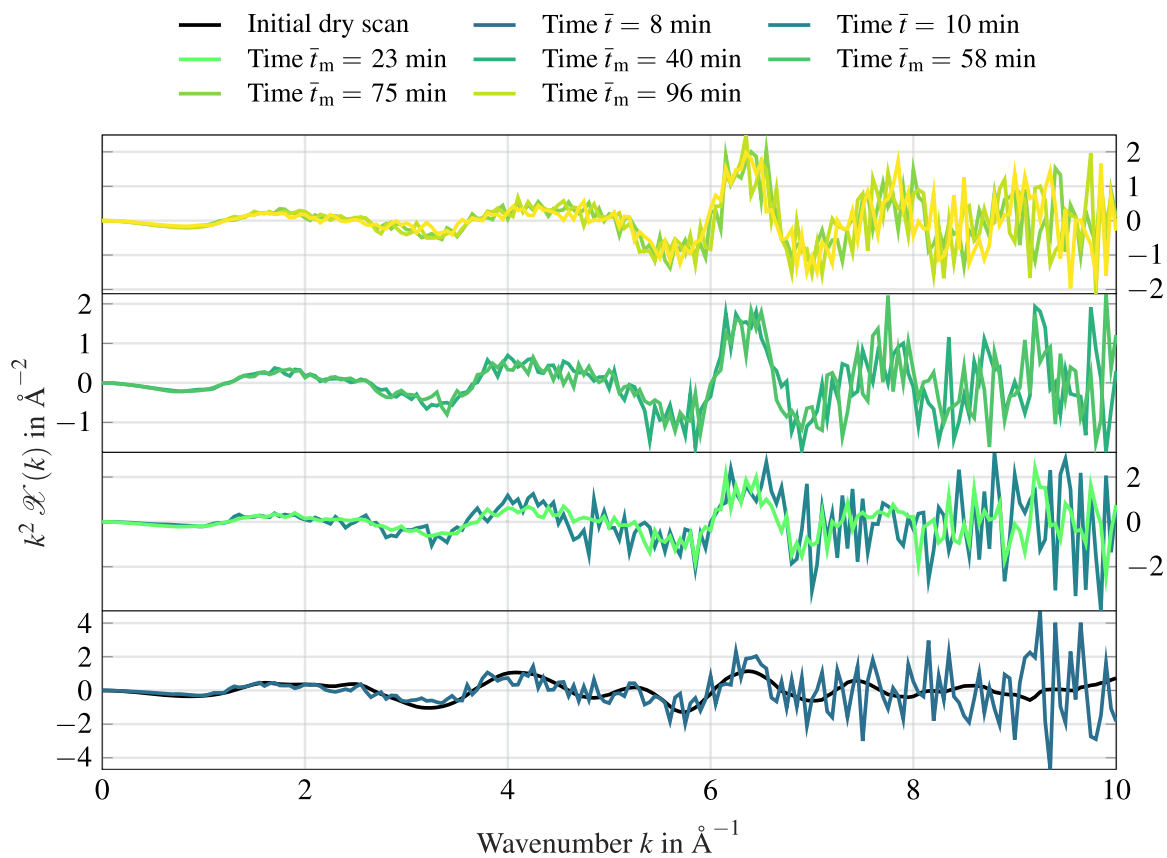


FIG. 47. k^2 -weighted $\chi(k)$ of Fig. 46.

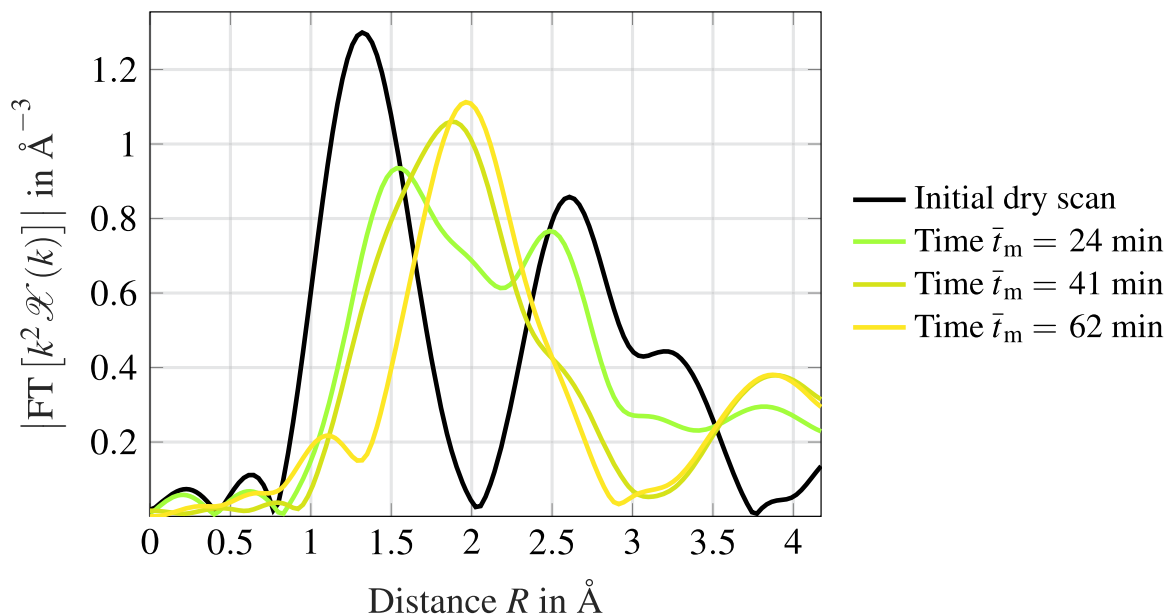


FIG. 48. Fourier transformed (k^2 -weighted) EXAFS data at the Fe K-edge of the γ -Fe₂O₃ particles during dissolution without light, all recorded in fluorescence mode (not corrected for phase shift).

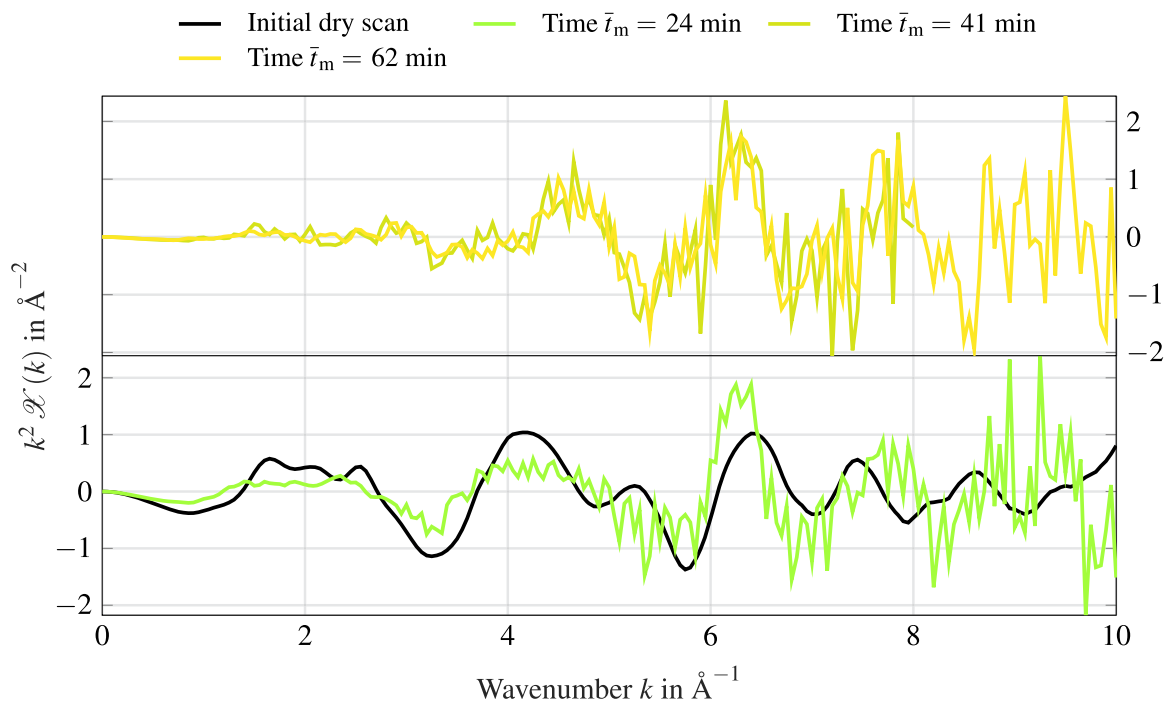


FIG. 49. k^2 -weighted $\chi(k)$ of Fig. 48.

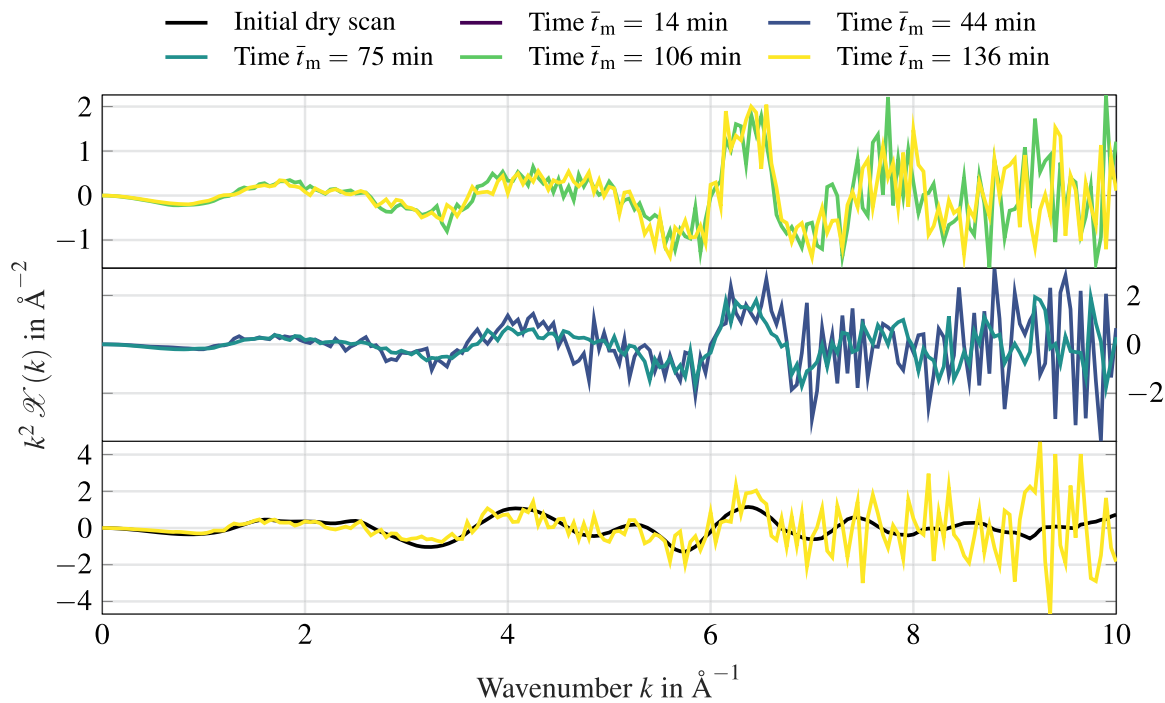


FIG. 50. k^2 -weighted $\chi(k)$ of Fig. 14.

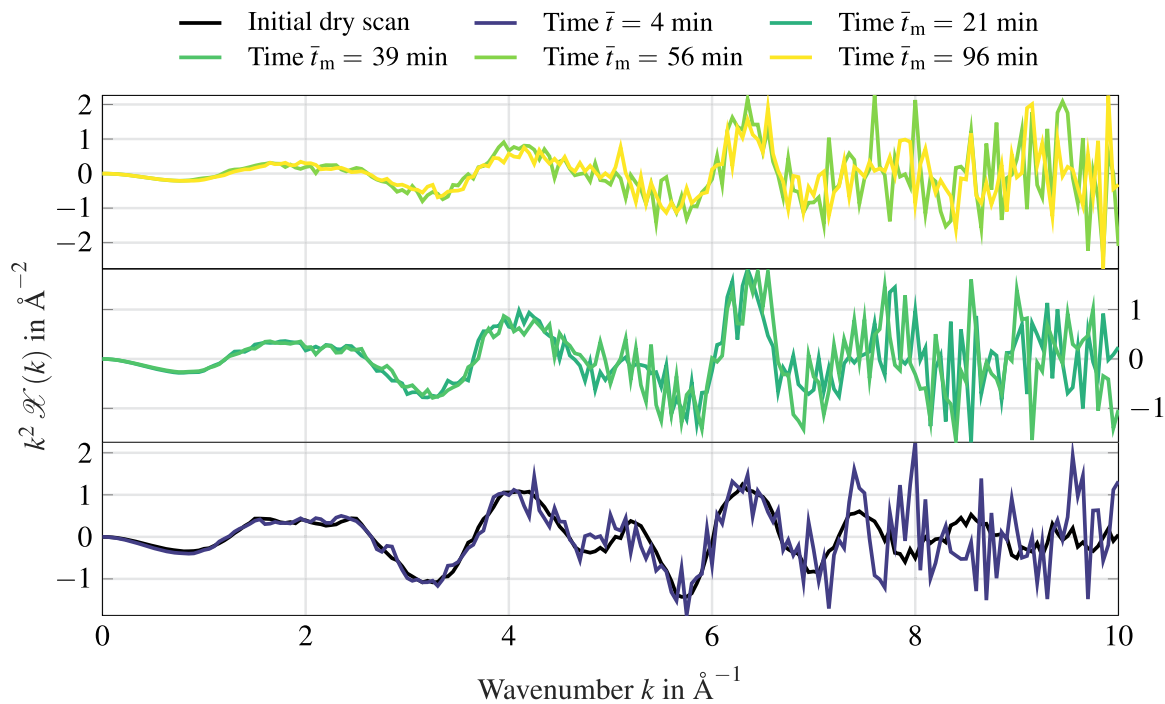


FIG. 51. k^2 -weighted $\chi(k)$ of Fig. 16.

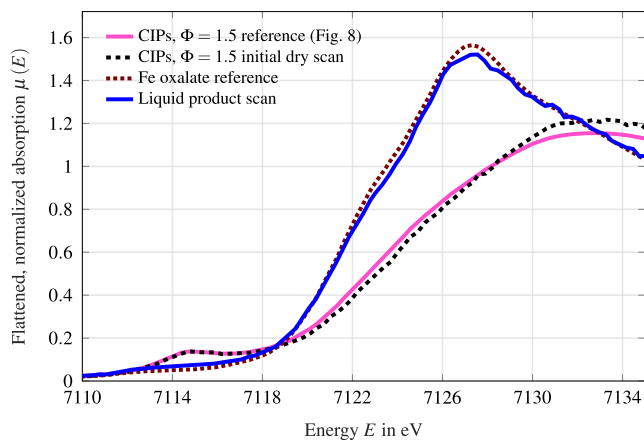


FIG. 52. XANES spectra of the liquid product and selected references after reaction with $\Phi = 1.5$ CIPs.

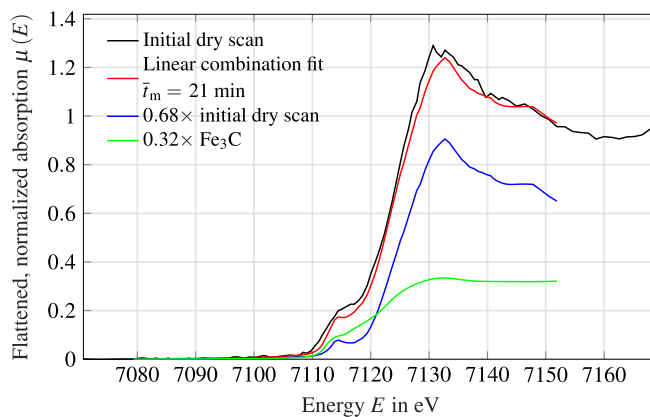


FIG. 54. Best fit of the first merged spectral data by means of LCA for the Fe₃O₄ dissolution experiment displayed in Fig. 15.

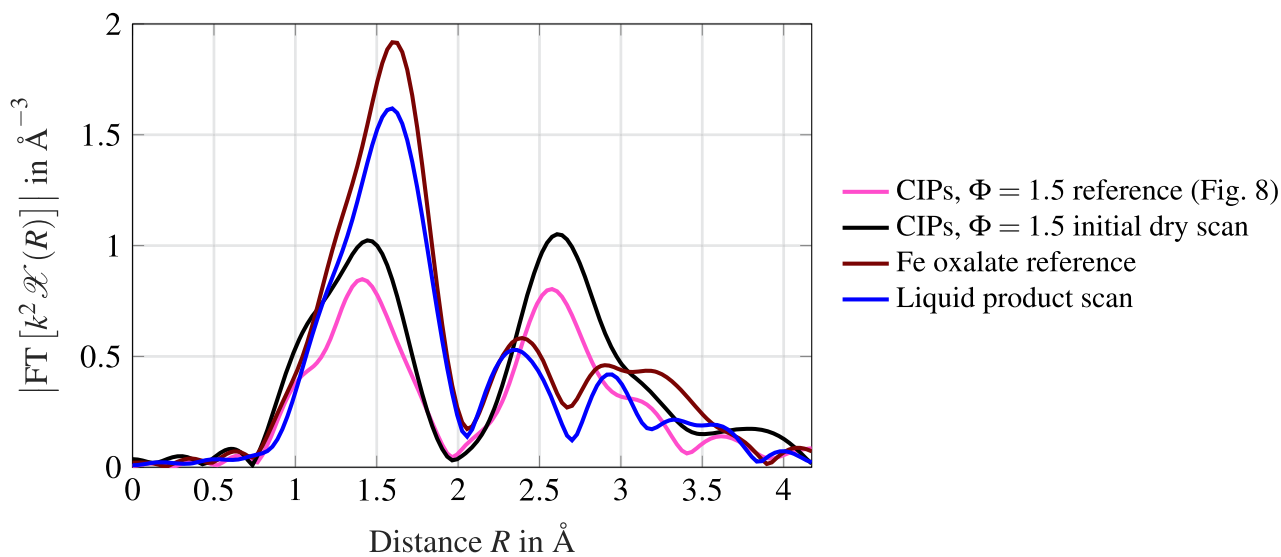


FIG. 53. Fourier transformed (k^2 -weighted) EXAFS data at the Fe K-edge of the liquid product and selected references after reaction with $\Phi = 1.5$ CIPs, all recorded in transmission mode (not corrected for phase shift).

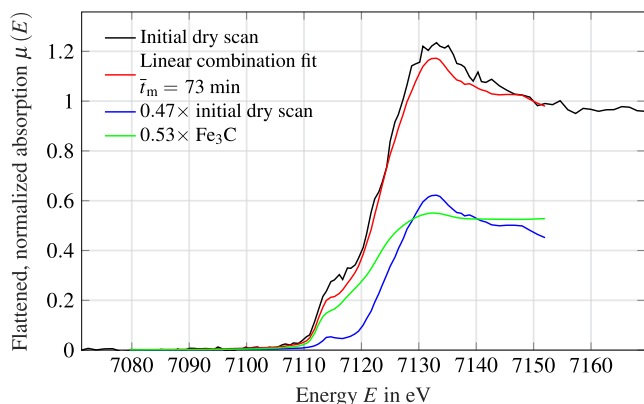


FIG. 55. Best fit of the final merged spectral data by means of LCA for the Fe_3O_4 dissolution experiment displayed in Fig. 15.

REFERENCES

- E. B. Borghi, S. P. Ali, P. J. Morando, and M. A. Blesa, "Cleaning of stainless steel surfaces and oxide dissolution by malonic and oxalic acids," *J. Nucl. Mater.* **229**, 115–123 (1996).
- K. A. Omar and R. Sadeghi, "Novel diglycolic acid-based deep eutectic solvents and their applications as a rust remover," *J. Mol. Liq.* **312**, 113380 (2020).
- W. Riemenschneider and M. Tanifuji, "Oxalic acid," in *Ullmanns Encyclopedia of Industrial Chemistry* (John Wiley & Sons, Ltd., 2011), Chap. 6, p. 537.
- Y. Chang, X. Zhai, B. Li, and Y. Fu, "Removal of iron from acidic leach liquor of lateritic nickel ore by goethite precipitate," *Hydrometallurgy* **101**, 84–87 (2010).
- R. K. Mishra, P. C. Rout, K. Sarangi, and K. C. Nathasarma, "Solvent extraction of Fe(III) from the chloride leach liquor of low grade iron ore tailings using Aliquat 336," *Hydrometallurgy* **108**, 93–99 (2011).
- M. Taxiarchou, D. Panias, I. Douni, I. Paspaliaris, and A. Kontopoulos, "Removal of iron from silica sand by leaching with oxalic acid," *Hydrometallurgy* **46**, 215–227 (1997).
- P. Debiagi, R. Rocha, A. Scholtiscek, J. Janicka, and C. Hasse, "Iron as a sustainable chemical carrier of renewable energy: Analysis of opportunities and challenges for retrofitting coal-fired power plants," *Renewable Sustainable Energy Rev.* **165**, 112579 (2022).
- M. Kueppers, W. Hall, P. Levi, R. Simon, and T. Vass, "Iron and steel," International Energy Agency, 2023, <https://www.iea.org/reports/iron-and-steel>.
- J. M. Bergthorson, S. Goroshin, M. J. Soo, P. Julien, J. Palecka, D. L. Frost, and D. J. Jarvis, "Direct combustion of recyclable metal fuels for zero-carbon heat and power," *Appl. Energy* **160**, 368–382 (2015).
- J. M. Bergthorson, "Recyclable metal fuels for clean and compact zero-carbon power," *Prog. Energy Combust. Sci.* **68**, 169–196 (2018).
- L. Dirven, N. G. Deen, and M. Golombok, "Dense energy carrier assessment of four combustible metal powders," *Sustainable Energy Technol. Assess.* **30**, 52–58 (2018).
- P. Julien and J. M. Bergthorson, "Enabling the metal fuel economy: Green recycling of metal fuels," *Sustainable Energy Fuels* **1**, 615–625 (2017).
- E. I. Shkolnikov, A. Z. Zhuk, and M. S. Vlaskin, "Aluminum as energy carrier: Feasibility analysis and current technologies overview," *Renewable Sustainable Energy Rev.* **15**, 4611–4623 (2011).
- H. Chen and V. H. Grassian, "Iron dissolution of dust source materials during simulated acidic processing: The effect of sulfuric, acetic, and oxalic acids," *Environ. Sci. Technol.* **47**, 10312–10321 (2013).
- S. O. Lee, T. Tran, B. H. Jung, S. J. Kim, and M. J. Kim, "Dissolution of iron oxide using oxalic acid," *Hydrometallurgy* **87**, 91–99 (2007).
- W. P. Miller, L. W. Zelazny, and D. C. Martens, "Dissolution of synthetic crystalline and noncrystalline iron oxides by organic acids," *Geoderma* **37**, 1–13 (1986).
- E. L. Smith, A. P. Abbott, and K. S. Ryder, "Deep eutectic solvents (DESS) and their applications," *Chem. Rev.* **114**, 11060–11082 (2014).
- R. M. Cornell and U. Schwertmann, "Dissolution," in *The Iron Oxides* (John Wiley & Sons, Ltd., 2003), Chap. 12, pp. 297–344.
- M. Lausch, P. Brockmann, F. Schmitt, B. Etzold, and J. Hussong, "In-situ iron oxide particle size and shape evolution during the dissolution in oxalic acid," *Chem. Eng. Sci.* **289**, 119864 (2024).
- Y. Lv, J. Liu, R. Zhu, J. Zhu, Q. Chen, X. Liang, and H. He, "Photoreductive dissolution of iron (hydr)oxides and its geochemical significance," *ACS Earth Space Chem.* **6**, 811–829 (2022).
- D. Panias, M. Taxiarchou, I. Paspaliaris, and A. Kontopoulos, "Mechanisms of dissolution of iron oxides in aqueous oxalic acid solutions," *Hydrometallurgy* **42**, 257–265 (1996).
- M. Taxiarchou, D. Panias, I. Douni, I. Paspaliaris, and A. Kontopoulos, "Dissolution of hematite in acidic oxalate solutions," *Hydrometallurgy* **44**, 287–299 (1997).
- M. I. Litter and M. A. Blesa, "Photodissolution of iron oxides. IV. A comparative study on the photodissolution of hematite, magnetite, and maghemite in EDTA media," *Can. J. Chem.* **70**, 2502–2510 (1992).
- W. Stumm, *Aquatic Surface Chemistry: Chemical Processes at the Particle-Water Interface* (John Wiley & Sons, 1987), Vol. 87.
- E. Baumgartner, M. Blesa, H. Marinovich, and A. J. G. Maroto, "Heterogeneous electron transfer as a pathway in the dissolution of magnetite in oxalic acid solutions," *Inorg. Chem.* **22**, 2224–2226 (1983).
- R. M. Sellers and W. J. Williams, "High-temperature dissolution of nickel chromium ferrites by oxalic acid and nitrilotriacetic acid," *Faraday Discuss. Chem. Soc.* **77**, 265–274 (1984).
- G. V. Buxton, T. Rhodes, and R. M. Sellers, "Radiation chemistry of colloidal haematite and magnetite in water. Reductive dissolution by $(\text{CH}_3)_2\text{COH}$ radicals and $\text{Fe}^{II}\text{EDTA}$," *J. Chem. Soc., Faraday Trans. 1* **79**, 2961–2974 (1983).
- D. M. Sherman, "Electronic structures of iron(III) and manganese(IV) (hydr)oxide minerals: Thermodynamics of photochemical reductive dissolution in aquatic environments," *Geochim. Cosmochim. Acta* **69**, 3249–3255 (2005).
- C. Siffert and B. Sulzberger, "Light-induced dissolution of hematite in the presence of oxalate. A case study," *Langmuir* **7**, 1627–1634 (1991).
- W. Stumm and B. Sulzberger, "The cycling of iron in natural environments: Considerations based on laboratory studies of heterogeneous redox processes," *Geochim. Cosmochim. Acta* **56**, 3233–3257 (1992).
- Z. K. Amirhosseini, R. Monsef, S. A. Ehsanzadeh, W. K. Y. Albahadly, H. S. Majdi, A. A. Amir, A. H. Dawood, and M. Salavati-Niasari, "Tailoring the photocatalytic activity of novel magnetically separable $\text{ZnFe}_{12}\text{O}_{19}$ -chitosan bionanocomposites: A green preparation, structural characterization and comparative study," *Int. J. Hydrogen Energy* **48**, 37286–37301 (2023).
- Z. Bielan, S. Dudziak, A. Kubiak, and E. Kowalska, "Application of spinel and hexagonal ferrites in heterogeneous photocatalysis," *Appl. Sci.* **11**, 10160 (2021).
- A. Jafarinejad, M. Salavati-Niasari, R. Monsef, and H. Bashiri, "Flower-shaped magnetically recyclable $\text{ZnS}/\text{ZnIn}_2\text{S}_4/\text{Fe}_2\text{O}_3$ nanocomposites towards decolorization of colored pollutants," *Int. J. Hydrogen Energy* **48**, 3440–3455 (2023).
- R. M. Kettler, D. J. Wesolowski, and D. A. Palmer, "Dissociation constants of oxalic acid in aqueous sodium chloride and sodium trifluoromethanesulfonate media to 175 °C," *J. Chem. Eng. Data* **43**, 337–350 (1998).
- D. Panias, M. Taxiarchou, I. Douni, I. Paspaliaris, and A. Kontopoulos, "Thermodynamic analysis of the reactions of iron oxides: Dissolution in oxalic acid," *Can. Metall. Q.* **35**, 363–373 (1996).
- P. Vehmaanperä, T. Sihvonen, R. Salmimies, and A. Häkkinen, "Dissolution of magnetite and hematite in mixtures of oxalic and nitric acid: Mechanisms and kinetics," *Minerals* **12**, 560 (2022).
- P. Santawaja, S. Kudo, A. Tahara, S. Asano, and J. ichiro Hayashi, "Dissolution of iron oxides highly loaded in oxalic acid aqueous solution for a potential application in iron-making," *ISIJ Int.* **62**, 2466 (2021).
- I. P. Pozdnyakov, O. V. Kel, V. F. Plyusnin, V. P. Grivin, and N. M. Bazhin, "New insight into photochemistry of ferrioxalate," *J. Phys. Chem. A* **112**, 8316–8322 (2008).

- ³⁹P. Vehmaanperä, B. Gong, P. Sit, R. Salmimies, B. Barbiellini, and A. Häkkinen, "Formation of humboldtine during the dissolution of hematite in oxalic acid—density functional theory (DFT) calculations and experimental verification," *Clays Clay Miner.* **69**, 655 (2021).
- ⁴⁰P. Santawaja, S. Kudo, A. Mori, A. Tahara, S. Asano, and J.-i. Hayashi, "Sustainable iron-making using oxalic acid: The concept, a brief review of key reactions, and an experimental demonstration of the iron-making process," *ACS Sustainable Chem. Eng.* **8**, 13292–13301 (2020).
- ⁴¹A. William, L. Dudeney, and I. I. Tarasova, "Photochemical decomposition of trisoxalatoiron(III): A hydrometallurgical application of daylight," *Hydrometallurgy* **47**, 243–257 (1998).
- ⁴²A. C. Lasaga and A. Lüttge, "A model for crystal dissolution," *Eur. J. Mineral.* **15**, 603–615 (2003).
- ⁴³N. Valverde and C. Wagner, "Considerations on the kinetics and the mechanism of the dissolution of metal oxides in acidic solutions," *Ber. Bunsengesellschaft Phys. Chem.* **80**, 330–333 (1976).
- ⁴⁴G. C. Allen, R. M. Sellers, and P. M. Tucker, "Surface composition and morphology of magnetite crystals during dissolution," *Philos. Mag.* **B 48**, L5–L9 (1983).
- ⁴⁵U. Schwertmann, "Solubility and dissolution of iron oxides," *Plant Soil* **130**, 1 (1991).
- ⁴⁶S. V. Yanina and K. M. Rosso, "Linked reactivity at mineral-water interfaces through bulk crystal conduction," *Science* **320**, 218–222 (2008).
- ⁴⁷T. Hiemstra and W. H. Van Riemsdijk, "Effect of different crystal faces on experimental interaction force and aggregation of hematite," *Langmuir* **15**, 8045–8051 (1999).
- ⁴⁸P. Joshi and C. A. Gorski, "Anisotropic morphological changes in goethite during Fe²⁺-catalyzed recrystallization," *Environ. Sci. Technol.* **50**, 7315–7324 (2016).
- ⁴⁹W. Stumm, G. Furrer, E. Wieland, and B. Zinder, "The effects of complex-forming ligands on the dissolution of oxides and aluminosilicates," in *The Chemistry of Weathering*, edited by J. I. Drever (Springer, Dordrecht, Netherlands, 1985), pp. 55–74.
- ⁵⁰M. I. Litter, E. C. Baumgartner, G. A. Urrutia, and M. A. Blesa, "Photodissolution of iron oxides. 3. Interplay of photochemical and thermal processes in maghemite/carboxylic acid systems," *Environ. Sci. Technol.* **25**, 1907–1913 (1991).
- ⁵¹E. Baumgartner, M. A. Blesa, and A. J. G. Maroto, "Kinetics of the dissolution of magnetite in thioglycolic acid solutions," *J. Chem. Soc., Dalton Trans.* **1982**, 1649.
- ⁵²M. A. Blesa, A. J. G. Maroto, and P. J. Morando, "Dissolution of cobalt ferrites by thioglycolic acid," *J. Chem. Soc., Faraday Trans. 1* **82**, 2345–2352 (1986).
- ⁵³V. I. E. Bruyère and M. A. Blesa, "Acidic and reductive dissolution of magnetite in aqueous sulfuric acid: Site-binding model and experimental results," *J. Electroanal. Chem. Interfacial Electrochem.* **182**, 141–156 (1985).
- ⁵⁴M. G. Segal and R. M. Sellers, "Kinetics of metal oxide dissolution. Reductive dissolution of nickel ferrite by tris(picolinato)vanadium(II)," *J. Chem. Soc., Faraday Trans. 1* **78**, 1149–1164 (1982).
- ⁵⁵P. Vehmaanperä, R. Salmimies, and A. Häkkinen, "Thermodynamic and kinetic studies of dissolution of hematite in mixtures of oxalic and sulfuric acid," *Min., Metall., Explor.* **38**, 69 (2020).
- ⁵⁶M. A. Blesa, H. A. Marinovich, E. C. Baumgartner, and A. J. G. Maroto, "Mechanism of dissolution of magnetite by oxalic acid-ferrous ion solutions," *Inorg. Chem.* **26**, 3713–3717 (1987).
- ⁵⁷R. Grau-Crespo, A. Y. Al-Baitai, I. Saadoun, and N. H. De Leeuw, "Vacancy ordering and electronic structure of γ -Fe₂O₃ (maghemite): A theoretical investigation," *J. Phys.: Condens. Matter* **22**, 255401 (2010).
- ⁵⁸T. Fujii, F. M. F. de Groot, G. A. Sawatzky, F. C. Voogt, T. Hibma, and K. Okada, "In situ XPS analysis of various iron oxide films grown by NO₂-assisted molecular-beam epitaxy," *Phys. Rev. B* **59**, 3195–3202 (1999).
- ⁵⁹D. Suter, S. Banwart, and W. Stumm, "Dissolution of hydrous iron(III) oxides by reductive mechanisms," *Langmuir* **7**, 809–813 (1991).
- ⁶⁰V. R. Ambikadevi and M. Lalithambika, "Effect of organic acids on ferric iron removal from iron-stained kaolinite," *Appl. Clay Sci.* **16**, 133–145 (2000).
- ⁶¹S. O. Lee, T. Tran, Y. Y. Park, S. J. Kim, and M. J. Kim, "Study on the kinetics of iron oxide leaching by oxalic acid," *Int. J. Miner. Process.* **80**, 144–152 (2006).
- ⁶²A. Martínez-Luévano, M. Rodríguez-Delgado, A. Uribe-Salas, F. Carrillo-Pedroza, and J. Osuna-Alarcón, "Leaching kinetics of iron from low grade kaolin by oxalic acid solutions," *Appl. Clay Sci.* **51**, 473–477 (2011).
- ⁶³H. Nakanishi, C. Sanchez, M. Hendewerk, and G. Somorjai, "Photochemical hydrogen production from a water-methanol mixture with small particles of iron oxide suspensions," *Mater. Res. Bull.* **21**, 137–148 (1986).
- ⁶⁴S. Buchheiser, M. P. Deutschmann, F. Rhein, A. Allmang, M. Fedoryk, B. Stelzner, S. Harth, D. Trimis, and H. Nirschl, "Particle and phase analysis of combusted iron particles for energy storage and release," *Materials* **16**, 2009 (2023).
- ⁶⁵L. Choizez, N. E. van Rooij, C. J. Hessels, A. K. da Silva, I. R. S. Filho, Y. Ma, P. de Goey, H. Springer, and D. Raabe, "Phase transformations and microstructure evolution during combustion of iron powder," *Acta Mater.* **239**, 118261 (2022).
- ⁶⁶X. Mi, A. Fujinawa, and J. M. Berghthorson, "A quantitative analysis of the ignition characteristics of fine iron particles," *Combust. Flame* **240**, 112011 (2022).
- ⁶⁷M. Fedoryk, B. Stelzner, S. Harth, and D. Trimis, "Experimental investigation of the laminar burning velocity of iron-air flames in a tube burner," *Appl. Energy Combust. Sci.* **13**, 100111 (2023).
- ⁶⁸D. Eggart, "Operando studies on iron and platinum based catalysts for the direct conversion of methane," Ph.D. thesis, Karlsruhe Institut für Technologie (KIT), 2022.
- ⁶⁹A. Zimina, K. Dardenne, M. A. Denecke, D. E. Doronkin, E. Huttel, H. Lichtenberg, S. Mangold, T. Pruessmann, J. Rothe, T. Spangenberg, R. Steininger, T. Vitova, H. Geckeis, and J.-D. Grunwaldt, "CAT-ACT—A new highly versatile x-ray spectroscopy beamline for catalysis and radionuclide science at the KIT synchrotron light facility ANKA," *Rev. Sci. Instrum.* **88**, 113113 (2017).
- ⁷⁰Institute for Beam Physics and Technology (IBPT), KIT-IBPT-Home, <https://www.ibpt.kit.edu/>, 2024.
- ⁷¹M. Newville, "Fundamentals of XAFS," *Rev. Mineral. Geochem.* **78**, 33–74 (2014).
- ⁷²I. J. Bruno, J. C. Cole, P. R. Edgington, M. Kessler, C. F. Macrae, P. McCabe, J. Pearson, and R. Taylor, "New software for searching the Cambridge Structural Database and visualizing crystal structures," *Acta Crystallogr., Sect. B: Struct. Sci.* **58**, 389–397 (2002).
- ⁷³C. F. Macrae, I. Sovago, S. J. Cottrell, P. T. A. Galek, P. McCabe, E. Pidcock, M. Platings, G. P. Shields, J. S. Stevens, M. Towler, and P. A. Wood, "Mercury 4.0: From visualization to analysis, design and prediction," *J. Appl. Crystallogr.* **53**, 226–235 (2020).
- ⁷⁴B. Ravel and M. Newville, "ATHENA and ARTEMIS: Interactive graphical data analysis using IFEFFIT," *Phys. Scr.* **2005**, 1007.
- ⁷⁵M. Newville, "Larch: An analysis package for XAFS and related spectroscopies," *J. Phys.: Conf. Ser.* **430**, 012007 (2013).
- ⁷⁶M. Newville, *Larch: Data Analysis Tools for X-Ray Spectroscopy* (The University of Chicago, 2022).
- ⁷⁷G. S. Henderson, F. M. de Groot, and B. J. Moulton, "3. X-ray absorption near-edge structure (XANES) spectroscopy," in *Spectroscopic Methods in Mineralogy and Material Sciences*, edited by G. Henderson, D. Neuville, and R. Downs (De Gruyter, Berlin, Boston, 2014), pp. 75–138.
- ⁷⁸A. Boubnov, H. Lichtenberg, S. Mangold, and J.-D. Grunwaldt, "Identification of the iron oxidation state and coordination geometry in iron oxide- and zeolite-based catalysts using pre-edge XAS analysis," *J. Synchrotron Radiat.* **22**, 410–426 (2015).
- ⁷⁹T. E. Westre, P. Kennepohl, J. G. DeWitt, B. Hedman, K. O. Hodgson, and E. I. Solomon, "A multiplet analysis of Fe K-edge 1s → 3d pre-edge features of iron complexes," *J. Am. Chem. Soc.* **119**, 6297–6314 (1997).
- ⁸⁰G. Calas and J. Petiau, "Coordination of iron in oxide glasses through high-resolution k-edge spectra: Information from the pre-edge," *Solid State Commun.* **48**, 625–629 (1983).
- ⁸¹L. Galois, G. Calas, and M. A. Arrio, "High-resolution XANES spectra of iron in minerals and glasses: Structural information from the pre-edge region," *Chem. Geol.* **174**, 307–319 (2001), part of the Special Issue: 6th International Silicate Melt Workshop.

- ⁸²D. A. Outka and J. Stöhr, "Curve fitting analysis of near-edge core excitation spectra of free, adsorbed, and polymeric molecules," *J. Chem. Phys.* **88**, 3539–3554 (1988).
- ⁸³S. Quartieri, M. P. Riccardi, B. Messiga, and F. Boscherini, "The ancient glass production of the medieval val Gargassa glasshouse: Fe and Mn XANES study," *J. Non-Cryst. Solids* **351**, 3013–3022 (2005).
- ⁸⁴H. Simon, G. Cibin, I. Freestone, and E. Schofield, "Fe K-edge x-ray absorption spectroscopy of corrosion phases of archaeological iron: Results, limitations, and the need for complementary techniques," *J. Phys.: Condens. Matter* **33**, 344002 (2021).
- ⁸⁵M. Wilke, F. Farges, P.-E. Petit, G. E. Brown, Jr., and F. Martin, "Oxidation state and coordination of Fe in minerals: An Fe K-XANES spectroscopic study," *Am. Mineral.* **86**, 714–730 (2001).
- ⁸⁶F. C. Hawthorne and G. A. Waychunas, "Chapter 3. Spectrum-fitting methods," in *Spectroscopic Methods in Mineralogy and Geology* (De Gruyter, Berlin, Boston, 1988), pp. 63–98.
- ⁸⁷M. Newville, P. Liviš, Y. Yacoby, J. J. Rehr, and E. A. Stern, "Near-edge x-ray-absorption fine structure of Pb: A comparison of theory and experiment," *Phys. Rev. B* **47**, 14126–14131 (1993).
- ⁸⁸K. Lagarec and D. G. Rancourt, *Recoil-Mössbauer Spectral Analysis Software for Windows* (University of Ottawa, Ottawa, ON, 1998), p. 43.
- ⁸⁹P. Scherrer, "Bestimmung der inneren Struktur und der Größe von Kolloidteilchen mittels Röntgenstrahlen," in *Kolloidchemie Ein Lehrbuch, Chemische Technologie in Einzeldarstellungen* (Springer, Berlin, Heidelberg, 1912), pp. 387–409.
- ⁹⁰G. Williamson and W. Hall, "X-ray line broadening from filed aluminium and wolfram," *Acta Metall.* **1**, 22–31 (1953).
- ⁹¹M. Ginder-Vogel and D. L. Sparks, "Chapter 1—The impacts of X-ray absorption spectroscopy on understanding soil processes and reaction mechanisms," in *Synchrotron-Based Techniques, Developments in Soil Science Vol. 34*, edited by B. Singh and M. Gräfe (Elsevier, 2010), pp. 1–26.
- ⁹²E. Murad and J. Cashion, *Mössbauer Spectroscopy of Environmental Materials and Their Industrial Utilization* (Springer Science & Business Media, 2011).
- ⁹³R. E. Vandenberghe and E. De Grave, "Application of Mössbauer spectroscopy in earth sciences," in *Mössbauer Spectroscopy: Tutorial Book* (Springer, Berlin, Heidelberg, 2013), pp. 91–185.
- ⁹⁴B. S. Clausen and H. Topsøe, "In-situ studies of catalysts by XAFS and Mössbauer spectroscopy," *Hyperfine Interact.* **47–48**, 203–217 (1989).
- ⁹⁵A. Burkhardt, T. Pakendorf, B. Reime, J. Meyer, P. Fischer, N. Stübe, S. Panneerselvam, O. Lorbeer, K. Stachnik, M. Warmer, P. Rödig, D. Göries, and A. Meents, "Status of the crystallography beamlines at PETRA III," *Eur. Phys. J. Plus* **131**, 56 (2016).
- ⁹⁶S. J. Oh, D. C. Cook, and H. E. Townsend, "Characterization of iron oxides commonly formed as corrosion products on steel," *Hyperfine Interact.* **112**, 59–66 (1998).
- ⁹⁷J. B. Mamani, L. F. Gamarra, and G. E. d. S. Brito, "Synthesis and characterization of Fe₃O₄ nanoparticles with perspectives in biomedical applications," *Mater. Res.* **17**, 542–549 (2014).
- ⁹⁸B. B. Sarma and J.-D. Grunwaldt, "Operando spectroscopy to understand dynamic structural changes of solid catalysts," *CHIMIA* **78**, 288–296 (2024).
- ⁹⁹B. Ravel and E. A. Stern, "Local disorder and near edge structure in titanate perovskites," *Physica B* **208–209**, 316–318 (1995), part of the Special Issue: Proceedings of the 8th International Conference on X-ray Absorption Fine Structure.
- ¹⁰⁰V. A. Shuvaeva, K. Yanagi, K. Yagi, K. Sakaue, and H. Terauchi, "Polarized XAFS study of the atomic displacements and phase transitions in KNbO₃," *J. Synchrotron Radiat.* **6**, 367–369 (1999).
- ¹⁰¹T. Vitova, M. R. Zamani-Meymian, K. Peithmann, K. Maier, and J. Hormes, "Atomic displacement and disorder in LiNbO₃ single crystal caused by high-energy ³He ion irradiation: An x-ray absorption spectroscopy study," *J. Phys.: Condens. Matter* **21**, 495401 (2009).
- ¹⁰²C. T. Chantler, "Theoretical form factor, attenuation, and scattering tabulation for Z = 1–92 from E = 1–10 eV to E = 0.4–1.0 MeV," *J. Phys. Chem. Ref. Data* **24**, 71–643 (1995).
- ¹⁰³C. T. Chantler, "Detailed tabulation of atomic form factors, photoelectric absorption and scattering cross section, and mass attenuation coefficients in the vicinity of absorption edges in the soft X-ray (Z = 30–36, Z = 60–89, E = 0.1–10 keV)—addressing convergence issues of earlier work," *J. Synchrotron Radiat.* **8**, 1124 (2001).
- ¹⁰⁴R. M. Cornell and U. Schwertmann, "Introduction to the iron oxides," in *The Iron Oxides* (John Wiley & Sons, Ltd, 2003), Chap. 1, pp. 1–7.
- ¹⁰⁵A. Espinosa, A. Serrano, A. Llavona, J. Jimenez de la Morena, M. Abuin, A. Figuerola, T. Pellegrino, J. F. Fernández, M. Garcia-Hernandez, G. R. Castro, and M. A. Garcia, "On the discrimination between magnetite and maghemite by XANES measurements in fluorescence mode," *Meas. Sci. Technol.* **23**, 015602 (2011).
- ¹⁰⁶B. Cortés-Llanos, A. Serrano, A. Muñoz-Noval, E. Urones-Garrote, A. del Campo, J. F. Marco, A. Ayuso-Sacido, and L. Pérez, "Thermal route for the synthesis of maghemite/hematite core/shell nanowires," *J. Phys. Chem. C* **121**, 23158–23165 (2017).
- ¹⁰⁷M. P. Fernández-García, P. Gorria, J. A. Blanco, A. B. Fuertes, M. Sevilla, R. Boada, J. Chaboy, D. Schmool, and J.-M. Grenèche, "Microstructure and magnetism of nanoparticles with γ -Fe core surrounded by α -Fe and iron oxide shells," *Phys. Rev. B* **81**, 094418 (2010).
- ¹⁰⁸A. Shavel, B. Rodríguez-González, M. Spasova, M. Farle, and L. M. Liz-Marzán, "Synthesis and characterization of iron/iron oxide core/shell nanocubes," *Adv. Funct. Mater.* **17**, 3870–3876 (2007).
- ¹⁰⁹A. Kuzmin and J. Chaboy, "EXAFS and XANES analysis of oxides at the nanoscale," *IUCr* **1**, 571–589 (2014).
- ¹¹⁰C. Piquer, M. A. Laguna-Marco, A. G. Roca, R. Boada, C. Guglieri, and J. Chaboy, "Fe k-edge x-ray absorption spectroscopy study of nanosized nominal magnetite," *J. Phys. Chem. C* **118**, 1332–1346 (2014).
- ¹¹¹F. M. Etzler and R. Deanne, "Particle size analysis: A comparison of various methods II," *Part. Part. Syst. Charact.* **14**, 278–282 (1997).
- ¹¹²F. M. Etzler and M. S. Sanderson, "Particle size analysis: A comparative study of various methods," *Part. Part. Syst. Charact.* **12**, 217–224 (1995).
- ¹¹³S. Li, D. Sanned, J. Huang, E. Berrocal, W. Cai, M. Aldén, M. Richter, and Z. Li, "Stereoscopic high-speed imaging of iron microexplosions and nanoparticle-release," *Opt. Express* **29**, 34465–34476 (2021).
- ¹¹⁴P. Tóth, Y. Ögren, A. Sepman, P. Gren, and H. Wiinikka, "Combustion behavior of pulverized sponge iron as a recyclable electrofuel," *Powder Technol.* **373**, 210–219 (2020).
- ¹¹⁵H. Wiinikka, T. Vikström, J. Wennebro, P. Toth, and A. Sepman, "Pulverized sponge iron, a zero-carbon and clean substitute for fossil coal in energy applications," *Energy Fuels* **32**, 9982–9989 (2018).
- ¹¹⁶J. G. Hering and W. Stumm, "Chapter 11. Oxidative and reductive dissolution of minerals," in *Mineral-Water Interface Geochemistry* (De Gruyter, Berlin, Boston, 1990), pp. 427–466.
- ¹¹⁷O. W. Duckworth and S. T. Martin, "Surface complexation and dissolution of hematite by C₁-C₆ dicarboxylic acids at pH = 5.0," *Geochim. Cosmochim. Acta* **65**, 4289–4301 (2001).
- ¹¹⁸R. Salmimies, P. Vehmaanperä, and A. Häkkinen, "Acidic dissolution of magnetite in mixtures of oxalic and sulfuric acid," *Hydrometallurgy* **163**, 91–98 (2016).
- ¹¹⁹F. m. c. Farges, G. E. Brown, and J. J. Rehr, "Ti K-edge XANES studies of Ti coordination and disorder in oxide compounds: Comparison between theory and experiment," *Phys. Rev. B* **56**, 1809–1819 (1997).
- ¹²⁰D. Larcher, D. Bonnin, R. Cortes, I. Rivals, L. Personnaz, and J.-M. Tarascon, "Combined XRD, EXAFS, and mössbauer studies of the reduction by lithium of α -Fe₂O₃ with various particle sizes," *J. Electrochem. Soc.* **150**, A1643 (2003).
- ¹²¹L. Signorini, L. Pasquini, L. Savini, R. Carboni, F. Boscherini, E. Bonetti, A. Giglia, M. Pedio, N. Mahne, and S. Nannarone, "Size-dependent oxidation in iron/iron oxide core-shell nanoparticles," *Phys. Rev. B* **68**, 195423 (2003).
- ¹²²H. I. Faraoun, Y. D. Zhang, C. Esling, and H. Aourag, "Crystalline, electronic, and magnetic structures of θ -Fe₃C, χ -Fe₃C₂, and η -Fe₂C from first principle calculation," *J. Appl. Phys.* **99**, 093508 (2006).
- ¹²³C. Nayak, N. Abharana, B. Modak, K. Halankar, S. N. Jha, and D. Bhattacharyya, "Insight into the charging–discharging of magnetite electrodes: In situ XAS and DFT study," *Phys. Chem. Chem. Phys.* **23**, 6051–6061 (2021).